

Tunable three dimensional shape changes in thermal-responsive liquid crystal thin films

A Project Report

submitted by

AKHIL REDDY PEEKETI

*in partial fulfilment of the requirements
for the award of the degree of*

BACHELOR OF TECHNOLOGY

in

MECHANICAL ENGINEERING

and

MASTER OF TECHNOLOGY

in

PRODUCT DESIGN



**DEPARTMENT OF MECHANICAL ENGINEERING
INDIAN INSTITUTE OF TECHNOLOGY MADRAS.**

MAY, 2019

PROJECT REPORT CERTIFICATE

This is to certify that the project report titled **Tunable three dimensional shape changes in thermal-responsive liquid crystal thin films**, submitted by **Akhil Reddy Peeketi** (ME14B116), to the Indian Institute of Technology, Madras, for the award of the degree of **Bachelor of Technology in Mechanical Engineering and Master of Technology in Product Design**, is a bonafide record of the research work done by him under my supervision. The contents of this thesis, in full or in parts, have not been submitted to any other Institute or University for the award of any degree or diploma.

Dr. Ratna Kumar Annabattula
Associate Professor & Guide
Dept. of Mechanical Engineering
Indian Institute of Technology Madras
Chennai - 600 036

Prof. N. Ramesh Babu
Head of the Department
Dept. of Mechanical Engineering
Indian Institute of Technology Madras
Chennai - 600 036

Place: Chennai

Date: 10 May, 2019

ACKNOWLEDGEMENTS

I am very grateful to my guide, Dr. Ratna Kumar A., IIT Madras, for providing me with all the guidance to complete the project. He supported me at needful times, teaching me concepts and methods while also motivating me to strive harder. He patiently guided me in the right direction throughout the course of the project. Without his encouragement and support, this project would not have been completed. I would like to extend my gratitude to Jeroen A.H.P Sol and Marina Pilz da Cunha, Technical University of Eindhoven (TU/e), The Netherlands, for carrying out the experiments and providing the data required for this work.

I would also like to thank the Machine Design Section, IIT Madras, the Stimuli-Responsive Systems (SRS) Laboratory and the Mechanics of Materials (MoM) Laboratory for high-performance computers and the software support, which enabled me to finish this project. Lastly, I would take this opportunity to thank my colleagues Kanishk Mehta, Raghuram K. Desu, Pramod Kumbhar and Adithya Ramgopal for many fruitful discussions during the course of the project and my family members for their constant and altruistic support at all times.

ABSTRACT

KEYWORDS: Liquid crystal thin films; stimuli-responsive; thermo-responsive; finite element modeling; rolling; rocking

The advent of responsive soft robots has revolutionized the field of robotics into a new era. Specifically, in the fields of energy harvesting, biotechnology and personal comfort, the stimuli-responsive actuators have begun playing a prominent role. Of different stimuli-responsive systems, liquid crystal (LC) polymers garner significant attention due to their ability to generate large strain and respond to diverse stimuli such as heat, light and chemicals. The liquid crystal thin films also offer greater flexibility to design the film for a desired actuation i.e., the shape change upon stimulus by varying the alignment distribution of the directors in the film. In this project, a computational methodology to predict the shape changes in the LC thin films for a given pre-determined spatial director alignment distribution is developed. The proposed methodology is validated by comparing the prediction result with the Timoshenko's analytical result of a thin bilayer film. Upon successful validation, the methodology is applied to design the thin films to generate multiple rolls by inducing thickness tapering along the length of the film. Also, the proposed methodology is used to simulate the rocking motion of a triangular thin film. The predictions of the proposed computational model show good correspondence with the experimental results. The computational model is further used to develop designs of thin films to generate cones and rolling wheels from tapered thin films. The developed finite element predictive model allows for exploration of possible actuation mechanisms leading to promising novel soft actuator designs to be produced experimentally.

Contents

ACKNOWLEDGEMENTS	i
ABSTRACT	iii
LIST OF FIGURES	viii
ABBREVIATIONS	ix
NOTATION	xi
1 Introduction	1
1.1 Liquid crystal polymer thin films	2
1.2 Literature review	2
1.3 Research gap and the objective	5
1.4 Overview of chapters	6
2 Finite element modeling of 3D shape changes in LC films	7
2.1 Constitutive equations	7
2.2 Spatial alignment distribution in ABAQUS	9
2.3 Validation	13
3 Development of tight rolling soft actuators by bio-mimicking the proboscis of butterfly	15
3.1 Introduction	15
3.2 Synthesis and characterization of LCN Films	16
3.3 Thermal response of tapered cantilever LCN films	20
3.4 Summary	22
4 Rock and roll motion of a thermo-responsive triangular LC film	25
4.1 Introduction	25
4.2 Synthesis and characterization of LCN films	27

4.3	Self-sustained Rocking	28
4.4	Summary	33
5	Summary and Future Scope	35
	LIST OF PAPERS BASED ON THE PROJECT	47

List of Figures

1.1	Schematic illustrating the different phases and director orientations in liquid crystal films (Liu and Broer, 2014)	3
1.2	Schematic illustrating the mechanical deformation induced due to the decrease in order of the molecules (Liu and Onck, 2018)	4
1.3	Different shape deformation observed in LCN films with different boundary conditions in response to light illumination.	4
1.4	The thermal response of nematic film with concentric and radial director orientations with constant orientation along the thickness but variant spatial director orientations (Ware <i>et al.</i> , 2015).	4
1.5	Formation of different shapes by designing the films with pre-determined spatial alignment distribution.	5
2.1	Comparison of radius of curvature estimated from the finite element results with that of the Timoshenko analytical formulation for a bilayer.	14
2.2	The finite element simulation results of the cases a) M1, b) M2, c) M3 and d) M4 respectively.	14
3.1	Schematics of the proboscis of butterfly and the developed tapered rectangular liquid crystal based soft actuator.	17
3.2	Differential scanning calorimetry of the LC mixture's phase behaviour. [source: (Sol <i>et al.</i> , 2019)]	18
3.3	Dynamic mechanical analysis (DMA) measurement performed on films of 20 μm thickness with planar alignment.	18
3.4	Scanning electron micrograph marking the different regions in the splay LCN film, as well as their penetration depths as function of the total film thickness. [source: (Sol <i>et al.</i> , 2019)]	19
3.5	Thermal strain in the parallel and perpendicular directions to the planar alignment of LCN film.	19
3.6	Comparison of experimental result of the shape of film with the finite element predictions.	20
3.7	A schematic showing the geometric conditions and film alignment distribution along the thickness used in the finite element model.	21
3.8	Plot comparing the radius of curvature estimated from experiments with the finite element predictions.	22

4.1	Schematic illustration of the unexpected rocking phenomena observed in triangular LCN film and the structures of monomers used for synthesis of LCN film.	27
4.2	Experimental measurement of coefficient of thermal expansion for parallel and perpendicular orientation of LCN film.	28
4.3	A plot of tip displacement of a rocking motion of triangular LCN film and snapshots at extremes	30
4.4	Influence of flattening temperature on the shape of the triangular LCN film	31
4.5	Results of finite element simulation of self-sustained rocking in triangular LCN film	32
4.6	Schematic of the mechanism for the self-sustained feedback loop for the triangular LCN	34
5.1	Alignment and tapering direction for the a) quarter circle and b) square film needed to generate cones.	35
5.2	Finite element simulation of a cone formation from a quarter circular tapered LCN film.	36
5.3	Finite element simulation of a cone formation from a Square diagonally tapered LCN film.	36
5.4	Schematic representation of formation of a wheel from a tapered rectangular LCN film	37
5.5	Forward motion of wheel made of tapered LCN film	38
5.6	Backward motion of wheel made of tapered LCN film	39

ABBREVIATIONS

LC	Liquid Crystal
LCN	Liquid Crystal polymer Network
LCE	Liquid Crystal Elastomer
LCD	Liquid Crystal Display
LCP	Liquid Crystal Polymer
FEM	Finite Element Modeling
DSC	Differential Scanning Calorimetry
POM	Polarized Optical Microscopy
DMA	Dynamic Mechanical Analysis
SEM	Scanning Electron Microscopy

NOTATION AND UNITS

E	Elastic modulus, MPa
ν	Poisson's ratio
G	Shear modulus, MPa
θ	Orientation angle in radians
γ	Spatial orientation angle in radians
r_c	Radius of curvature, mm
T_g	Glass transition temperature, °C
T_f	Flattening temperature, °C
A_t	Threshold value for amplitude of oscillations, mm
t	Thickness of film, μm
d_o	Thickness at thicker end, μm
d_i	Thickness at thinner end, μm
d_{avg}	average thickness, μm
T	Temperature, °C
x, y, z	Coordinates
m	Ratio of elastic moduli
l	Length, mm
w	Width, mm
\mathbf{u}	Displacement vector, mm
$\boldsymbol{\sigma}$	Stress tensor, MPa
$\boldsymbol{\varepsilon}$	Strain tensor
α	Thermal expansion coefficient tensor, K^{-1}
\mathbf{C}	Elasticity tensor, MPa
\mathbf{T}	Transformation matrix
\mathbf{R}	Reuter's matrix
\mathbf{S}	Rotation matrix
$p_i, p = l, m, n$ $i = 1, 2, 3$	Components of rotation matrix \mathbf{S}
Superscripts	
t	thermal
e	elastic
\mathbf{T}	transpose
Subscripts	
0	reference
i, j, k, l	indices
N-I	Nematic to Isotropic

Chapter 1

Introduction

Stimuli-responsive materials have gained considerable attention in the recent times owing to their potential applications in fields such as soft robotics, medical diagnostics and aerospace industry (Ganta *et al.*, 2008; Meng and Li, 2013; Wei *et al.*, 2017; Ziolkowski *et al.*, 2013) among others. A wide-range of stimuli namely heat, light, electrical, magnetic and chemical sources have been shown to trigger responses in different material systems. The range of responses could vary from change in material's micro-structure to macroscopic deformation as well as change in material's intrinsic properties. The changes in shape are of great interest to the fields like soft-robotics as such responsive systems can be used to develop mechanical actuators such as soft-grippers, caterpillar-like inching robots removing the dependency on conventional motors for actuation. Of many available stimuli-responsive material systems, liquid crystal polymers have garnered significance due to their versatility and the capability to engineer the material system for a specific task. Also, liquid crystal thin films have been reported to show large mechanical strains in response to multiple external stimuli such as light, heat and chemical media (Broer *et al.*, 2011; White and Broer, 2015; Woltman *et al.*, 2007).

Liquid crystals (LCs), are distinguished as a class of smart materials at the end of nineteenth century. Since, then these material systems have raised the curiosity of many researchers world-wide leading to the application of liquid crystals in different fields. One well-known application of liquid crystal systems is the "Liquid-Crystal Displays (LCDs)", an integral part of all the current generation electronic display devices. These materials exhibit long-range positional or orientational order at the molecular level. This positional or orientational order can be changed from a fully ordered system - "crystalline phase" to a fully disordered system - "isotropic/liquid phase", thus the term 'liquid crystal'. The application of LCs in display devices has created a detailed understanding of these material systems, thereby, leading to more applications beyond displays, such as solar-energy harvesting, soft-robotics, photonics, bio-medicine, and microfluidics.

1.1 Liquid crystal polymer thin films

Polymer systems displaying liquid crystalline nature have been classified mainly as liquid crystal polymers (LCPs), liquid crystal polymer networks (LCNs) and liquid crystal elastomers (LCEs) based on their chemical composition and the cross-linking density. LCPs have very high moduli (> 100 GPa) with melting temperature as high as 300 °C and shows negligible change in the order upon heating. LCNs are moderately to densely cross-linked resulting in moduli of $1\text{--}2$ GPa with a glass transition temperatures (T_g) in the range of $40\text{--}120$ °C and they exhibit moderate changes in order upon heating. LCEs have low cross-linking density and thereby shows large changes in order unlike LCNs and LCPs and a low moduli of $0.1\text{--}5$ MPa. Since, LCEs exhibit large changes in order, they also show large mechanical strains compared to LCNs and LCPs.

The liquid crystals exhibit different crystalline phases such as nematic, smectic and liquid isotropic phase. Nematic phase corresponds to liquid crystals with rod like organic molecules with no positional order but self-aligned to have a long range directional order. On the other hand, smectic phase consists of molecules with certain positional order forming well defined layers that can slide over one another. Also, the molecular order of the liquid crystal materials can be classified into two types: *homeotropic* where the director is perpendicular to the substrate plane and the *planar* where the director is parallel to the substrate plane. The molecular order along the thickness can be varied resulting in films with various director distributions like twisted nematic, splayed nematic, chiral nematic (Broer *et al.*, 2011). A schematic depicting the different phases and molecular orders is shown in Fig. 1.1. The liquid crystal materials demonstrate phase transformations based on the intensity of the stimulus such as temperature (thermotropic), light (phototropic) and chemical concentration (lyotropic). The macroscopic shape and topology changes are strongly coupled with the director distribution across the films.

1.2 Literature review

The mechanical strains developed in both LCNs and LCEs are strongly linked to the direction of molecular alignment and the phase. LCEs undergo phase transformation

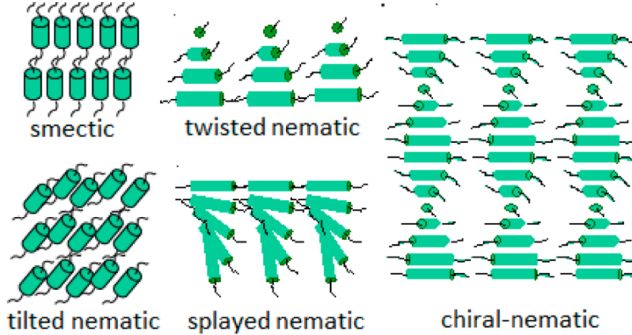


Figure 1.1: Schematic illustrating the different phases and director orientations in liquid crystal films (Liu and Broer, 2014)

from nematic to isotropic (or paranematic) resulting in a contraction along the initial director orientation and expansion perpendicular to the orientation as represented in the Fig. 1.2. LCNs retain the alignment order below their decomposition temperature due to high crosslinking density than the LCEs. LCNs also show contractions along the director orientation and expansion along the direction perpendicular to the director, but smaller in magnitude than that of LCEs. For instance, Fig. 1.3a shows the response of a cantilever LCN film with twisted nematic director orientation when subjected to UV radiation. Upon excitation with UV light, the different director orientations along the thickness result in strain gradient due to which the film bends resembling a bimetallic strip. On the contrary, when the bottom surface of the film is tightly bonded to a stiff substrate, surface topographical deformations as reported in (Liu and Broer, 2017; McConney *et al.*, 2013) can be realized. An example for surface deformations is presented in Fig. 1.3b for a LCN film with a periodic pattern of chiral nematic and homeotropic alignments. Complex shape deformations such as twist, curl, conical and origami inspired shapes can be realized by controlling the spatial orientations of the film, initial geometry of the film and the boundary conditions (de Haan *et al.*, 2014a; Mol *et al.*, 2005; Pei *et al.*, 2014; Ryu *et al.*, 2012; White, 2017). For example, the thermal response of LCE fixed at the center with directors parallel to concentric circles and radial arrangement shows different forms of cone as observed in Fig. 1.4. A few examples of origami inspired shapes obtained through external stimuli in polymer films can be seen in Fig. 1.5.

From the discussion presented above, it may be concluded that the alignment of directors together with the film geometry and the boundary conditions play a critical roles in the geometry of the deformed LCN/LCE films. The alignment order of the

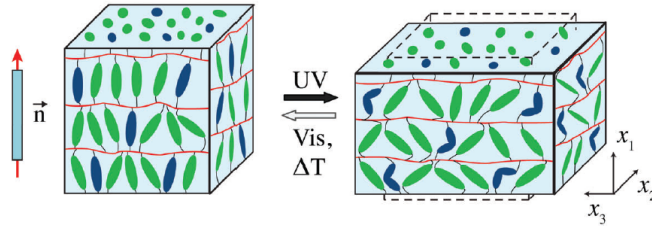


Figure 1.2: Schematic illustrating the mechanical deformation induced due to the decrease in order of the molecules (Liu and Onck, 2018)

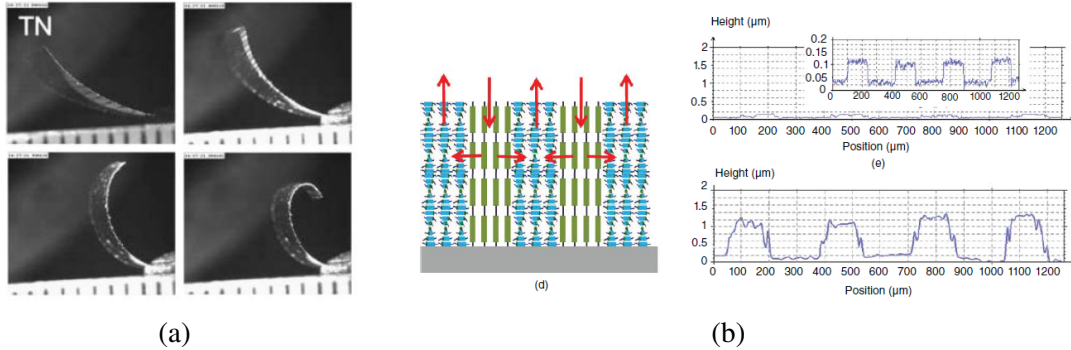


Figure 1.3: (a) The photo-response of a twisted nematic thin film showing bending as a result of strain gradient along the thickness generated by the variation of director orientation along the thickness (Warner *et al.*, 2010). (b) The surface topographical deformations for a patterned film with periodic homeotropic and chiral nematic orientations (Liu and Broer, 2017).

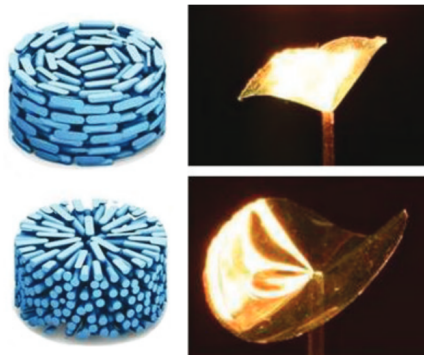


Figure 1.4: The thermal response of nematic film with concentric and radial director orientations with constant orientation along the thickness but variant spatial director orientations (Ware *et al.*, 2015).

liquid crystal films can be controlled through different methods such as mechanical stretching, surface alignment and photo alignment (de Haan *et al.*, 2014a; Pei *et al.*, 2014; White and Broer, 2015). The surface alignment technique allows us to vary the orientation along the thickness by specifying the orientations for the top and bottom layers. The spatial control of these orientations can be achieved through various external stimuli alignment tools (de Haan *et al.*, 2014a; Pei *et al.*, 2014; Ware *et al.*, 2015).

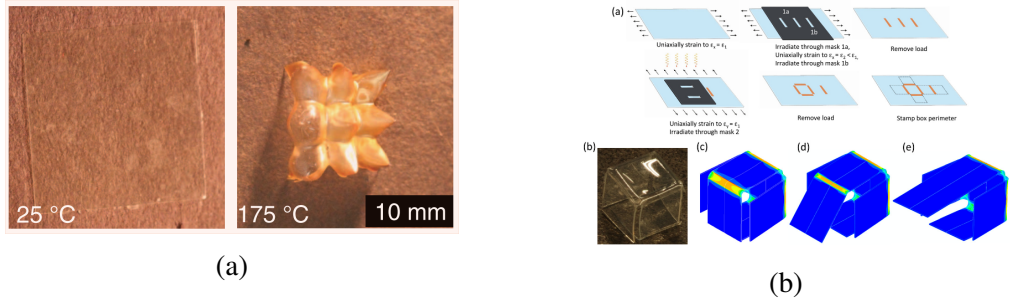


Figure 1.5: (a) The thermal response of a film with the pattern of circular alignments resulting in a pattern of cones inspired by origami (Ware *et al.*, 2015). (b) Origami inspired box formation using photo-induced strain gradient in polymer films (Ryu *et al.*, 2012)

Today, it is possible to have an extreme control over the spatial resolution of the directors resulting in a voxel volume as minimum as 0.0005 mm^3 (Ware *et al.*, 2015). Such a precise control over the spatial and through thickness variation of the director orientation in liquid crystal films enables us to realize numerous reversible complex three dimensional shapes.

1.3 Research gap and the objective

Although, it has been shown in the literature that an extreme control over the spatial resolution of the director orientation is possible, it is still not clear which combination of director orientations, film geometry and boundary conditions results in which geometrical shape. Also, the optimal director distribution and the boundary conditions needed to realize a given shape are still ambiguous. Hence, it would be interesting if a computational model becomes available to determine the probable three-dimensional deformation for a given combination of three-dimensional alignment distribution and geometrical characteristics. The computational model could then be used to create a data-set linking possible alignment and boundary conditions with the corresponding probable shape deformations. The optimal alignment and boundary conditions can then be used in accordance with the existing orientation programming set-ups (de Haan *et al.*, 2014a; Ware *et al.*, 2015) to develop films with specified spatial director distributions that are ideal for a desired shape change. Thus, the objectives of our work based on the current research gaps in the literature are

1. Development of a computational model considering the through thickness varia-

tion of alignment and planar variation of alignment and different boundary conditions.

2. Application of the developed model for predicting shape changes for different director distributions and boundary conditions to aid the experiments.

1.4 Overview of chapters

The formulation of the predictive finite element model with the implementation of the spatial alignment distribution and the subsequent validation of the model is presented in Chapter 2. Application of the methodology developed to assist the experiments making designed shape deformations and motions is presented in Chapters 3 and 4. Chapter 5 summarizes the work and presents the future scope for the applications of the developed methodology.

Chapter 2

Finite element modeling of 3D shape changes in LC films

2.1 Constitutive equations

A one way coupled thermo-mechanical model is developed to simulate the behaviour of LC thin films in a commercial finite element software ABAQUS (Smith, 2009). The constitutive equations to implement the thermo-mechanical model are presented in the following.

The thermal strain developed due to the temperature change can be formulated as,

$$\varepsilon_{ij}^t = \alpha_{ij}\Delta T, \quad (2.1.1)$$

where, ε_{ij}^t is the thermal strain tensor, α_{ij} is the thermal expansion coefficient tensor and ΔT is the temperature change. The liquid crystal polymer materials are transversely isotropic in nature with a rotational symmetry along the director orientation. Upon heating, the order of the system decreases as the mesogens start re-orienting. As a direct result of this, these materials show expansion in the direction perpendicular to the director and contraction in the direction parallel to the director as illustrated in the Fig. 1.2. Hence, the thermal expansion coefficient tensor will have two independent values - parallel to the director α_{11} and perpendicular to the director $\alpha_{22} = \alpha_{33}$. As the material expands in the direction perpendicular to the director, $\alpha_{22} = \alpha_{33} > 0$ and as the material contracts along the director, $\alpha_{11} < 0$.

The total strain is estimated as the sum of the elastic and thermal strains as,

$$\varepsilon_{ij} = \varepsilon_{ij}^e + \varepsilon_{ij}^t, \quad (2.1.2)$$

where, ε_{ij} is the total strain and ε_{ij}^e is the elastic strain. Now, assuming a linear stress-strain relationship, the stress in Voigt notation can be written as,

$$\sigma_{ij} = C_{ijkl}\varepsilon_{ij}^e = C_{ijkl}(\varepsilon_{ij} - \varepsilon_{ij}^t), \quad (2.1.3)$$

where, σ_{ij} is the stress tensor and C_{ijkl} is the elasticity tensor. The elasticity tensor for an orthotropic system can be written in the form presented below (Smith, 2009),

$$C_{ijkl} = \begin{bmatrix} C_{1111} & C_{1122} & C_{1133} & 0 & 0 & 0 \\ & C_{2222} & C_{2233} & 0 & 0 & 0 \\ & & C_{3333} & 0 & 0 & 0 \\ & & & C_{1212} & 0 & 0 \\ & sym & & & C_{1313} & 0 \\ & & & & & C_{2323} \end{bmatrix} \quad (2.1.4)$$

where the terms can be estimated from the engineering constants as,

$$\begin{aligned} C_{1111} &= E_{11}(1 - \nu_{23}\nu_{32})\Gamma \\ C_{2222} &= E_{22}(1 - \nu_{13}\nu_{31})\Gamma \\ C_{3333} &= E_{33}(1 - \nu_{12}\nu_{21})\Gamma \\ C_{1122} &= E_{11}(\nu_{21} + \nu_{31}\nu_{23})\Gamma = E_{22}(\nu_{12} + \nu_{32}\nu_{13})\Gamma \\ C_{1133} &= E_{11}(\nu_{31} + \nu_{21}\nu_{32})\Gamma = E_{33}(\nu_{13} + \nu_{12}\nu_{23})\Gamma \\ C_{2233} &= E_{22}(\nu_{32} + \nu_{12}\nu_{31})\Gamma = E_{33}(\nu_{23} + \nu_{21}\nu_{13})\Gamma \\ C_{1212} &= G_{12} \\ C_{1313} &= G_{13} \\ C_{2323} &= G_{23} \end{aligned}$$

$$\text{and } \Gamma = \frac{1}{1 - \nu_{12}\nu_{21} - \nu_{23}\nu_{32} - \nu_{13}\nu_{31} - 2\nu_{21}\nu_{32}\nu_{13}}.$$

Due to the transverse isotropic nature of LC polymers, they generally have five independent engineering constants as follows (Liu and Onck, 2018),

1. the elastic modulus parallel to the director \mathbf{n} - E_{11} ,
2. the elastic moduli perpendicular to the director \mathbf{n} - $E_{22} = E_{33}$,
3. the Poisson's ratios $\nu_{12} = \nu_{13}$,
4. the Poisson's ratio inside the isotropic plane ν_{23} and
5. the shear moduli parallel to the director \mathbf{n} $G_{12} = G_{13}$.

The remaining three Poisson's ratios can be estimated as,

$$\begin{aligned} \nu_{21} &= \frac{E_{22}}{E_{11}}\nu_{12}, \\ \nu_{31} &= \frac{E_{33}}{E_{11}}\nu_{13} \quad \text{and} \\ \nu_{32} &= \frac{E_{33}}{E_{22}}\nu_{23}. \end{aligned}$$

The shear modulus perpendicular to the director \mathbf{n} - G_{23} can be estimated as $E_{22}/(2(1 + \nu_{23}))$. The stress-strain equation in full form turns out as,

$$\begin{bmatrix} \sigma_{11} \\ \sigma_{22} \\ \sigma_{33} \\ \sigma_{12} \\ \sigma_{13} \\ \sigma_{23} \end{bmatrix} = \begin{bmatrix} C_{1111} & C_{1122} & C_{1133} & 0 & 0 & 0 \\ & C_{2222} & C_{2233} & 0 & 0 & 0 \\ & & C_{3333} & 0 & 0 & 0 \\ & & & C_{1212} & 0 & 0 \\ & & & & C_{1313} & 0 \\ & & & & & C_{2323} \end{bmatrix} \begin{bmatrix} \varepsilon_{11} \\ \varepsilon_{22} \\ \varepsilon_{33} \\ \varepsilon_{12} \\ \varepsilon_{13} \\ \varepsilon_{23} \end{bmatrix} \quad (2.1.5)$$

Once the stress-strain relationship is established and their values estimated, the system can solved for equilibrium as,

$$\sigma_{ij,j} = 0, \quad (2.1.6)$$

where $(\cdot)_j$, j represents $\partial(\cdot)/\partial x_j$. The model incorporates geometrically nonlinear deformation to simulate the system with large rotation but with small strains. Hence the Green-Lagrangian strain formulation is considered for the strain (ε) as,

$$\varepsilon = \frac{1}{2}(\nabla \mathbf{u} + \nabla \mathbf{u}^T + \nabla \mathbf{u}^T \nabla \mathbf{u}), \quad (2.1.7)$$

where \mathbf{u} corresponds to the displacement. The dependency of elastic moduli and the expansion coefficients on the temperature can also be implemented. As discussed in the earlier chapters, the LC films can exhibit variation in alignment through thickness as well as in the plane of the film. This spatial variation of the alignment is implemented as presented in the following section.

2.2 Spatial alignment distribution in ABAQUS

Finite element modeling of thin films is usually performed using “shell” elements in ABAQUS (Smith, 2009). The through thickness variation of the alignment can be specified by using a composite shell with multiple layers in a specified ratio (Smith, 2009). Using this composite shell, splayed nematic and twisted nematic orientational alignments can be modeled directly. Based on the orientation of the layer, the layer proper-

ties i.e, the elasticity tensor C and the thermal expansion coefficient tensor α needs to be estimated. As the elastic moduli and thermal expansion depend on the director orientation \mathbf{n} , the corresponding layers' properties such as C and α need to be transformed into the global coordinate system. For instance, consider a splayed nematic alignment with the director \mathbf{n} parallel to X-axis at the planar side, the director \mathbf{n} rotates about Y-axis through the thickness and transforms to homeotropic alignment (\mathbf{n} parallel to Z-axis).

Assume x', y', z' as the global coordinate system and x, y, z as the local coordinate system. Assume σ' and ε' as the global stress and strain tensors and σ and ε are the stress and strain tensors in local coordinate system in Voigt notation. Let T be the transformation matrix for transforming σ to σ' i.e.,

$$\sigma' = T\sigma, \quad (2.2.1)$$

where T is given as,

$$T = \begin{bmatrix} l_1^2 & m_1^2 & n_1^2 & 2l_1m_1 & 2l_1n_1 & 2m_1n_1 \\ l_2^2 & m_2^2 & n_2^2 & 2l_2m_2 & 2l_2n_2 & 2m_2n_2 \\ l_3^2 & m_3^2 & n_3^2 & 2l_3m_3 & 2l_3n_3 & 2m_3n_3 \\ l_1l_2 & m_1m_2 & n_1n_2 & l_1m_2 + l_2m_1 & l_1n_2 + l_2n_1 & m_1n_2 + m_2n_1 \\ l_1l_3 & m_1m_3 & n_1n_3 & l_1m_3 + l_3m_1 & l_1n_3 + l_3n_1 & m_1n_3 + m_3n_1 \\ l_2l_3 & m_2m_3 & n_1n_3 & l_2m_3 + l_3m_2 & l_2n_3 + l_3n_2 & m_2n_3 + m_3n_2 \end{bmatrix} \quad (2.2.2)$$

where l_i , $i = 1, 2, 3$, m_i , $i = 1, 2, 3$ and n_i , $i = 1, 2, 3$ are the components of the rotation matrix S . For example, if the transformation is the rotation of coordinate systems by angle θ about Y-axis (as in the case of splayed nematic film), the the rotation matrix S is given by,

$$S = \begin{bmatrix} l_1 & m_1 & n_1 \\ l_2 & m_2 & n_2 \\ l_3 & m_3 & n_3 \end{bmatrix} = \begin{bmatrix} \cos \theta & 0 & \sin \theta \\ 0 & 1 & 0 \\ -\sin \theta & 0 & \cos \theta \end{bmatrix} \quad (2.2.3)$$

In similar with stress transformation, strain tensor can be transformed as,

$$\begin{bmatrix} \varepsilon'_{11} \\ \varepsilon'_{22} \\ \varepsilon'_{33} \\ \varepsilon'_{12}/2 \\ \varepsilon'_{13}/2 \\ \varepsilon'_{23}/2 \end{bmatrix} = \mathbf{T} \begin{bmatrix} \varepsilon_{11} \\ \varepsilon_{22} \\ \varepsilon_{33} \\ \varepsilon_{12}/2 \\ \varepsilon_{13}/2 \\ \varepsilon_{23}/2 \end{bmatrix} \quad (2.2.4)$$

Using the Reuters' matrix (\mathbf{R}) defined as,

$$\mathbf{R} = \begin{bmatrix} 1 & 0 & 0 & 0 & 0 & 0 \\ 0 & 1 & 0 & 0 & 0 & 0 \\ 0 & 0 & 1 & 0 & 0 & 0 \\ 0 & 0 & 0 & 2 & 0 & 0 \\ 0 & 0 & 0 & 0 & 2 & 0 \\ 0 & 0 & 0 & 0 & 0 & 2 \end{bmatrix} \quad (2.2.5)$$

strain tensor can be written as,

$$\begin{bmatrix} \varepsilon'_{11} \\ \varepsilon'_{22} \\ \varepsilon'_{33} \\ \varepsilon'_{12} \\ \varepsilon'_{13} \\ \varepsilon'_{23} \end{bmatrix} = \mathbf{R} \begin{bmatrix} \varepsilon'_{11} \\ \varepsilon'_{22} \\ \varepsilon'_{33} \\ \varepsilon'_{12}/2 \\ \varepsilon'_{13}/2 \\ \varepsilon'_{23}/2 \end{bmatrix} = \mathbf{R}\mathbf{T} \begin{bmatrix} \varepsilon_{11} \\ \varepsilon_{22} \\ \varepsilon_{33} \\ \varepsilon_{12}/2 \\ \varepsilon_{13}/2 \\ \varepsilon_{23}/2 \end{bmatrix} = \mathbf{R}\mathbf{T}\mathbf{R}^{-1} \begin{bmatrix} \varepsilon_{11} \\ \varepsilon_{22} \\ \varepsilon_{33} \\ \varepsilon_{12} \\ \varepsilon_{13} \\ \varepsilon_{23} \end{bmatrix}. \quad (2.2.6)$$

Now the strain transformation can be written as

$$\boldsymbol{\varepsilon}' = \mathbf{R}\mathbf{T}\mathbf{R}^{-1}\boldsymbol{\varepsilon}. \quad (2.2.7)$$

If α' and α are the expansion coefficient tensors in Voigt notation, i.e.,

$$\begin{bmatrix} \varepsilon'_{11} \\ \varepsilon'_{22} \\ \varepsilon'_{33} \\ \varepsilon'_{12} \\ \varepsilon'_{13} \\ \varepsilon'_{23} \end{bmatrix} = \Delta T \begin{bmatrix} \alpha'_{11} \\ \alpha'_{22} \\ \alpha'_{33} \\ \alpha'_{12} \\ \alpha'_{13} \\ \alpha'_{23} \end{bmatrix} \quad \text{and} \quad \begin{bmatrix} \varepsilon_{11} \\ \varepsilon_{22} \\ \varepsilon_{33} \\ \varepsilon_{12} \\ \varepsilon_{13} \\ \varepsilon_{23} \end{bmatrix} = \Delta T \begin{bmatrix} \alpha_{11} \\ \alpha_{22} \\ \alpha_{33} \\ \alpha_{12} \\ \alpha_{13} \\ \alpha_{23} \end{bmatrix}, \quad (2.2.8)$$

then, using above equation,

$$\alpha' \Delta T = \mathbf{R} \mathbf{T} \mathbf{R}^{-1} \alpha \Delta T.$$

Hence, the thermal expansion coefficient tensor in the global coordinate system can be obtained from the transformation of the local expansion coefficient tensor as below,

$$\alpha' = \mathbf{R} \mathbf{T} \mathbf{R}^{-1} \alpha. \quad (2.2.9)$$

Now, consider C' and C as the elasticity tensors in the global and local coordinate systems. In the global coordinate system, the stress-strain relationship can be written as,

$$\begin{aligned} \sigma' &= C' \varepsilon' \\ \implies \mathbf{T} \sigma &= C' \mathbf{R} \mathbf{T} \mathbf{R}^{-1} \varepsilon \\ \implies \mathbf{T} \mathbf{C} \varepsilon &= C' \mathbf{R} \mathbf{T} \mathbf{R}^{-1} \varepsilon \\ \implies (\mathbf{T} \mathbf{C} - C' \mathbf{R} \mathbf{T} \mathbf{R}^{-1}) \varepsilon &= 0 \\ \implies C' \mathbf{R} \mathbf{T} \mathbf{R}^{-1} &= \mathbf{T} \mathbf{C} \\ \implies C' &= \mathbf{T} \mathbf{C} (\mathbf{R} \mathbf{T} \mathbf{R}^{-1})^{-1} \end{aligned} \quad (2.2.10)$$

Using the methodology of transformation discussed till now, we can estimate the global elasticity tensor C' and global thermal expansion coefficients α' for any given local orientation. Examples of this will be shown in later sections of this chapter as well as in next chapters.

The usual method to model in plane variation of alignment is to divide the film into multiple partitions and specify the alignment accordingly. But in LC polymer network

films, the in-plane variation change happens over small length scales which makes it impossible to manually select each zone and then specifying alignment. An innovative way to solve this issue is to specify the alignment for each element in the ABAQUS input file using an external algorithm. In this work, MATLAB is used to modify the ABAQUS input file accordingly. For instance, to specify a concentric alignment as illustrated in the Fig. 1.4, the orientation angle (γ_i) of each element i can be calculated as,

$$\gamma_i = \tan^{-1} \left(\frac{\bar{y}_i - y_0}{\bar{x}_i - x_0} \right), \quad (2.2.11)$$

where \bar{x}_i and \bar{y}_i are the mean of x and y coordinates of all the nodes of element i , x_0 and y_0 represent the center of concentric alignment distribution. The orientation angle θ_i can be specified for each element i in ABAQUS input file and thus implementing the concentric alignment distribution of the LC film.

2.3 Validation

The finite element model is validated by comparing the results for planar/homeotropic bilayer thin films against the analytical solution derived by Timoshenko (Timoshenko, 1925) for a bilayer film. For a bilayer film with total thickness as H and equal layer thicknesses, the radius of curvature r_c can be estimated as,

$$r_c = \frac{H(m + m^{-1} + 14)}{(24(\alpha_1 - \alpha_2)\Delta T)}. \quad (2.3.1)$$

Here, $m = (E_1(1 - \nu_1))/(E_2(1 - \nu_2))$ and E_i , ν_i and α_i ($i = 1, 2$) are the elastic modulus, Poisson's ratio and the coefficient of thermal expansion, respectively for the layer i and ΔT is the change in temperature. Finite element simulations are performed with different values of m and different mesh element sizes for a bilayer tapered film of length 20 mm, width 5 mm and thickness as 50 μm at the fixed edge and 20 μm at the free edge. Comparison of the radius of curvatures estimated from the finite element simulations with that of the analytical solution shows good correspondence as seen in Fig. 2.1 for different cases M1, M2, M3 and M4.

- M1: $E_1 = E_2 = 1000$ MPa, mesh element size = 0.2 mm
- M2: $E_1 = E_2 = 1000$ MPa, mesh element size = 0.05 mm

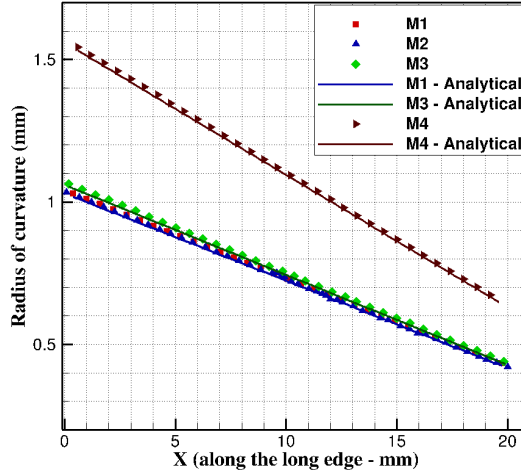


Figure 2.1: Comparison of radius of curvature estimated from the finite element results with that of the Timoshenko analytical formulation for a bilayer.

- M3: $E_1 = 2E_2$ with $E_1 = 1000$ MPa, $E_2 = 500$ MPa, mesh element size = 0.1 mm
- M4: $E_1 = 10E_2$ with $E_1 = 1000$ MPa, $E_2 = 100$ MPa, mesh element size = 0.1 mm

For the simulations, the values of thermal expansion coefficients are taken as $\alpha_1 = -0.000090 / \text{K}$, $\alpha_2 = 0.000270 / \text{K}$, the temperature change is taken as $\Delta T = 90^\circ\text{C}$ and the Poisson's ratio is taken as $\nu_1 = \nu_2 = 0.3$.

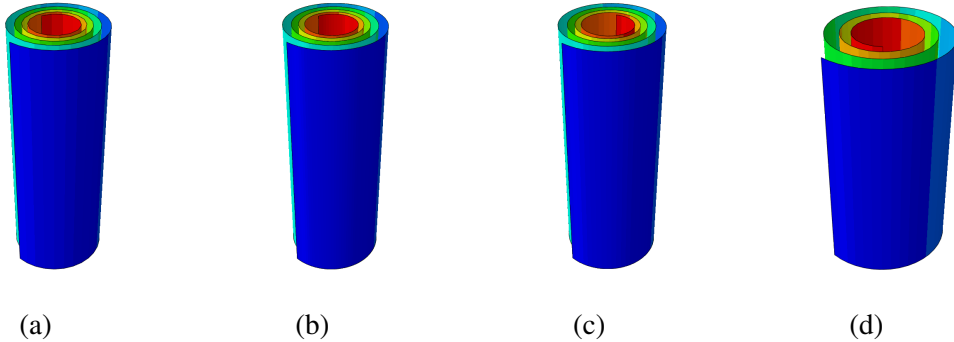


Figure 2.2: The finite element simulation results of the cases a) M1, b) M2, c) M3 and d) M4 respectively.

The finite element methodology adopted for the above discussed bilayer film is extended to model the thermal response of an actual liquid crystal thin film with splayed nematic orientation (alignment changes from homeotropic to planar through the thickness) in the following chapter.

Chapter 3

Development of tight rolling soft actuators by bio-mimicking the proboscis of butterfly

Note: This chapter is partially reproduced from the authors' published work (Sol et al., 2019).

3.1 Introduction

The world of robotics is at a point of revolution—soft robots are poised to challenge for supremacy. In particular, in the fields of sustainable energy harvesting (Gelebart *et al.*, 2017a), biomedical engineering (Cianchetti *et al.*, 2018) and personal comfort (Visschers *et al.*, 2018)—these remotely-addressable yet compliant materials are making great strides towards becoming the constituents of choice for many smart devices to come. For soft robotics researchers, the natural world is a great source of inspiration (Aßhoff *et al.*, 2017; van Oosten *et al.*, 2009; Wallin *et al.*, 2018; Wani *et al.*, 2017; Zeng *et al.*, 2018a). Nature provides insights into many of the solutions to engineering problems facing soft robotics today: microrobots based on bacteria (Palagi and Fischer, 2018) and electrospun water strider legs (Bai *et al.*, 2014) are two examples of using natural blueprints to generate novel man-made devices.

One of the prime candidate materials for bio-inspired soft robots is liquid crystal networks (LCNs), which are densely crosslinked polymers built up of reactive self-assembling monomers (“reactive mesogens”) (Lahikainen *et al.*, 2018; Zeng *et al.*, 2018b). The significance of LCNs in these developments is largely based on their anisotropic thermo-mechanical behaviour—upon disordering, LCNs shrink along the molecular director **n**, while they expand perpendicular to **n** (Mol *et al.*, 2005). LCNs have been used to create biomimetic soft actuators: caterpillar-like inching robots (Zeng *et al.*, 2018a), Venus flytrap-inspired grippers (Wani *et al.*, 2017), high-power seedpod actuators (Aßhoff *et al.*, 2017), or, inspired by the locomotion of micro-organisms, “microrobots” (Nocentini *et al.*, 2017; Zeng *et al.*, 2015).

Remarkably, all LCN-based actuators reported to date feature a uniform film thickness. Recently, a tapered paper–polyester bilayer was reported in which the tapered structure showed neat rolling and could be used to grapple objects.¹⁶ However, in this case, the polyester acted as a shape memory material, meaning that autonomous actuation can only be performed once—in contrast to actuators based on LCNs, which are known to exhibit reversible motion (Mol *et al.*, 2005).

Previously shown splay-LCNs of constant film thickness typically bend up to a full rotation at elevated temperatures (Mol *et al.*, 2005). In this work, LCNs are made with a thickness taper along the length of the film, similar to the proboscis of butterflies, their feeding organ (see Fig. 3.1a for a comparison) (Krenn and Kristensen, 2004; Krenn and Mühlberger, 2002). At rest, it is coiled up under their head, taking up minimal space. In action, it can extend to the body length of the butterfly and is used to retrieve nectar from plants or nutrients from rotting fruits, depending on the species of butterfly (Krenn, 2010). Our proboscis-inspired tapered actuators show tight bending behaviour unique in splay-LCNs, with up to $3\frac{1}{2}$ rotations upon heating or exposure to light. This rolling is fully reversible to reveal a nearly straight polymer strip at room temperature. Finite element modelling (FEM) results correspond well with experimental results. This allows for reversing the roles in the future, where the finite element model can be harnessed to anticipate the response of yet unexplored LC alignments and film geometries. Eventually, this could find use in designing LCN actuators that perform complex functions in larger soft robotic assemblies, or possibly as stand-alone devices in mixing systems for microfluidics.

3.2 Synthesis and characterization of LCN Films

Tapered-thickness, splay-aligned LCN thin films are obtained by filling alignment cells with a liquid crystal mixture consisting of equal weight fractions of monoacrylate 1 and diacrylate crosslinker 2 (see Fig. 3.1d for structures). Photo-activated actuation is achieved through the incorporation of azobenzene dye 3, which covalently bonds to the LCN during photo-polymerisation. Photo-initiation of the free radical polymerisation is accomplished by 4. The phase behaviour of the mixture was studied by differential scanning calorimetry (DSC) and polarised optical microscopy (POM). These results in-

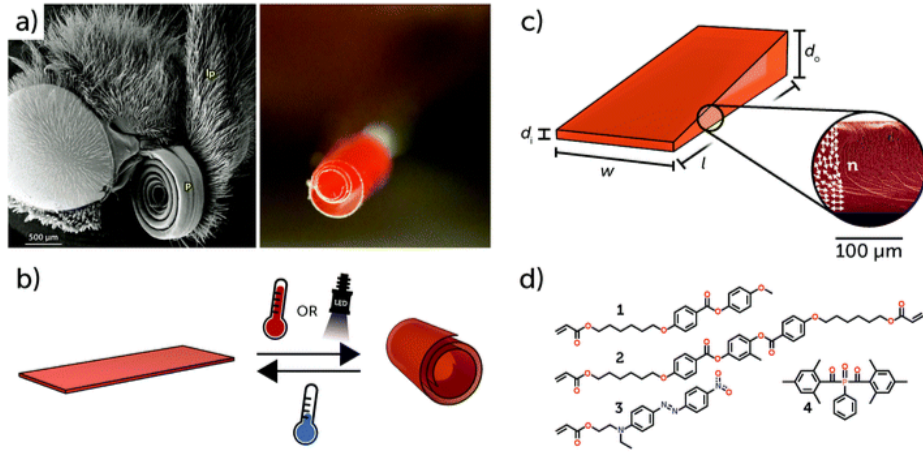


Figure 3.1: (a) (Left) Head of a *Vanessa cardui* butterfly featuring its proboscis (p) in the resting position (Krenn, 2010). (Right) A tightly rolled tapered LCN film as described in this chapter. (b) Schematic of the tapered actuator film concept; upon temperature increase or by irradiating with 455 nm light, the splay LCN rolls into a proboscis-like shape. When the light source is removed or the temperature is decreased, the sample unrolls. (c) Schematic showing the shape of a tapered LCN, depicting the molecular alignment n and other film characteristics such as the aspect ratio l/w and thicknesses d_i and d_o . Inset: Cross-section of a high-thickness splay-aligned LCN, featuring the molecular director (white arrows) as a function of film depth. (d) Reactive mesogens 1–3 and photo-initiator 4 used to fabricate the liquid crystalline network actuator. [source: (Sol *et al.*, 2019)]

dicate an isotropic to nematic transition at 77°C ($T_{\text{N-I}}$) when cooling, see Fig. 3.2 for details. Splay-aligned LC cells were made by sticking together glass with homeotropic and rubbed planar polyimide alignment layers facing each other. Spacer glue ($10\ \mu\text{m}$) and double-sided tape ($50\ \mu\text{m}$) were used to provide an LC alignment cell with a tapered cell gap. These cells were filled with the LC mixture at 90°C , above $T_{\text{N-I}}$. After filling, the temperature was lowered to 55°C , whereupon the LCs self-assembled into a nematic mesophase. After photo-initiated co-polymerisation to lock in the monomer's alignment, a thermal post-curing ensured maximum conversion of the acrylate groups. DSC reveals that the phase transition peak at $T_{\text{N-I}}$ has disappeared after polymerisation, as expected (see Fig. 3.2). Cells were opened using a razor blade, revealing a thin film stuck to the glass coated with planar-aligned polyimide. Surface profilometry determined that film thicknesses were close to the spacer diameters chosen during cell manufacture. Furthermore, the thickness gradient between the thin and thick sides was linear. A polarised optical micrograph verified that the uniaxial nematic alignment was fixed during polymerisation, and dynamic mechanical analysis (DMA) revealed that the LCN has a broad glass transition range with the peak of $\tan(\delta)$ (= ratio of storage

to loss modulus) at around 65°C (T_g , Fig. 3.3). Scanning electron micrographs confirm that even at film thicknesses exceeding 100 mm, splay alignment is retained (see Fig. 1c). The estimated ratios of penetration depth between homeotropic- and planar-aligned mesogens through the depth of the film depend on the film thickness (see Fig. 3.4). The thermal response of the nematic system is characterized as the total thermal strain generated while heating from a given reference temperature and presented in Fig. 3.5.

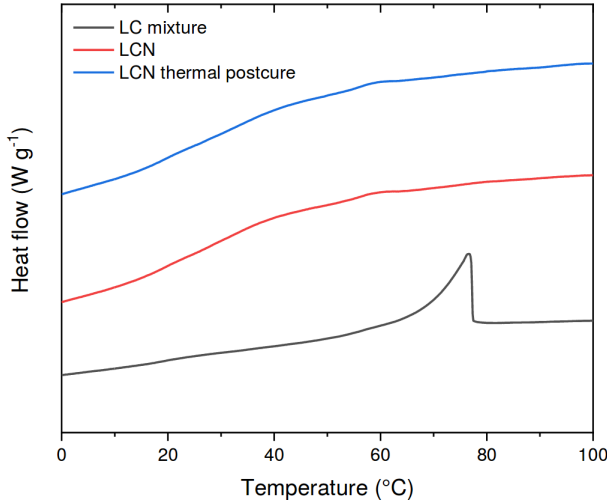


Figure 3.2: Differential scanning calorimetry of the LC mixture's phase behaviour.
[source: (Sol *et al.*, 2019)]

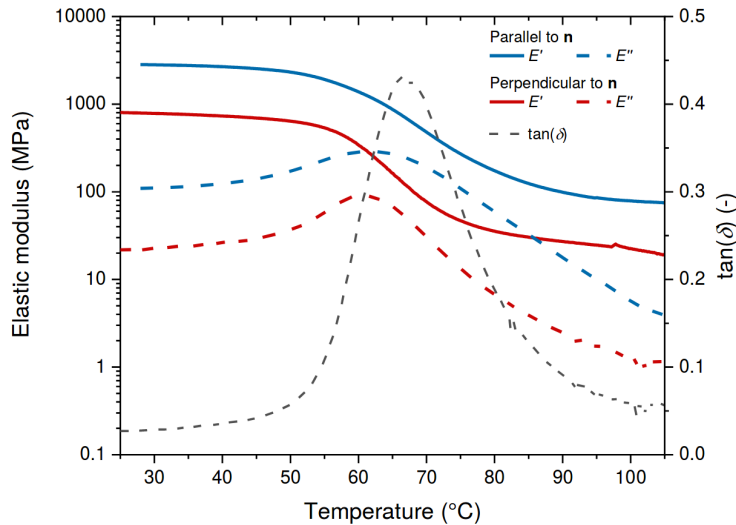


Figure 3.3: Dynamic mechanical analysis (DMA) measurement performed on films of $20\ \mu\text{m}$ thickness with planar alignment. Plotted as function of temperature: Storage modulus (E') and Loss modulus (E'') for parallel (E_{11} , blue) and perpendicular ($E_{22} = E_{33}$, red) to \mathbf{n} , as well as dissipation factor $\tan(\delta)$.
[source: (Sol *et al.*, 2019)]

Films were cut from the LCN as a strip with a $\Delta d = d_o - d_i = 20\ \text{mm}$, $d_{\text{avg}} = 25\ \text{mm}$, $l/w = 4$ and the thickness taper Δd in the same direction as the nematic director \mathbf{n}

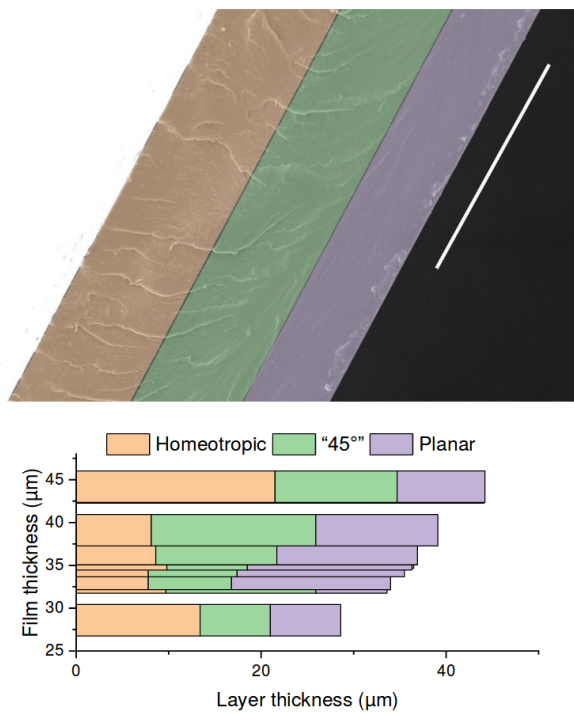


Figure 3.4: Scanning electron micrograph marking the different regions in the splay LCN film, as well as their penetration depths as function of the total film thickness. [source: (Sol *et al.*, 2019)]

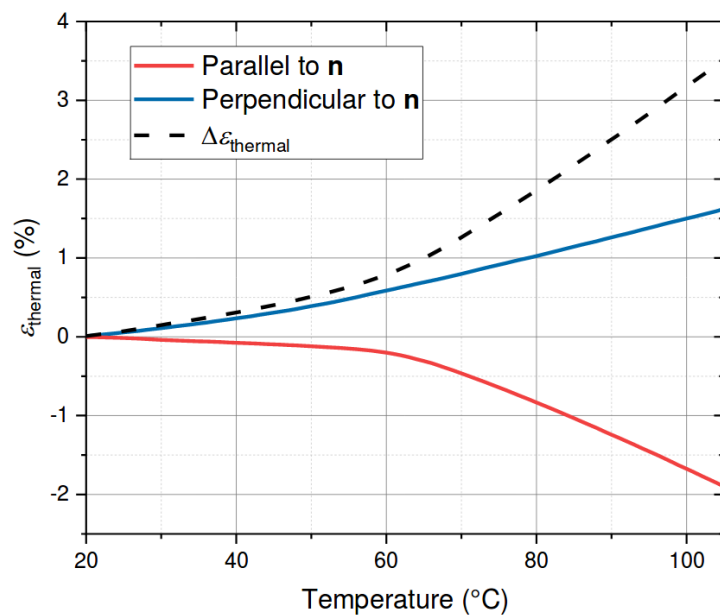


Figure 3.5: Thermal strain for directions \mathbf{n} parallel to the strain analyser direction (ε_{11}), \mathbf{n} perpendicular to the strain analyser ($\varepsilon_{22}=\varepsilon_{33}$), and the difference ($\Delta\varepsilon$) as function of the temperature. The values are calculated with reference point $T_0 = 19$ °C. [source: (Sol *et al.*, 2019)]

(see Fig. 3.1c for a schematic image detailing these parameters). Upon removal of this film from the glass substrate, a free-standing film is obtained that shows no to little pre-bend, in which case the film slightly bends with the homeotropic side inward. This can be explained by the lower polymerisation temperature, which pre-empts the build-up of large thermal strains during polymerisation, and the thermal annealing, which also alleviates thermal stresses (Verpaalen *et al.*, 2018).

3.3 Thermal response of tapered cantilever LCN films

The free-standing films were actuated in an oven with a window, through which photographs were recorded at set intervals. A digital temperature sensor recorded the temperature inside the oven at the same intervals. As the temperature was increased to 100 °C, the film rolled up tightly, with a curvature of several hundreds of degrees. This is best visualised in a series of photographs, as in Fig. 3.6. This behaviour can be explained with Timoshenko's model for bimetallic strips in mind, which correlates film thickness with the radius of curvature (r_c) for a given differential thermal strain (Timoshenko, 1925). In splay-aligned films with planar anchoring on one face of the film and homeotropic on the other, curling is observed typically up to a full rotation at elevated temperatures (Mol *et al.*, 2005). Compared to this earlier work the tapered films show an increasingly smaller r_c over their length, allowing them to effectively roll into themselves.

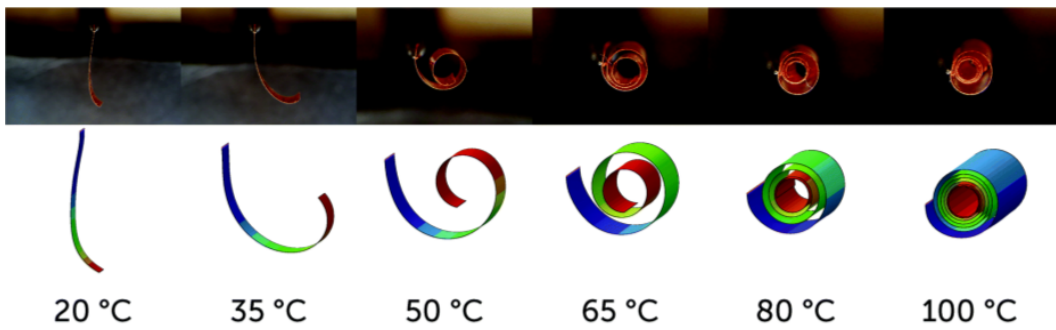


Figure 3.6: Comparison of experimental thermo-mechanical bending results (top) with finite element method results (bottom) for a tapered splay-aligned LCN film at different temperatures. Coloured regions in the finite element results correspond to the increasing value of curvature ($1/r_c$) from blue to red. [source: (Sol *et al.*, 2019)]

In order to better understand the bending behaviour of these tapered thickness LCNs,

finite element simulations were performed. As described in more detail in the Chapter 2, the tapered geometry along the length of the film is discretised using four noded shell elements with composite sectional properties for the finite element model. The properties of the elastic moduli and the thermal expansion as a function of temperature were measured and used as input for the model (see Figs. 3.3 and 3.5). The finite element model incorporates the variation in the LC alignment direction through the depth of the film, thus making it a functionally graded system. The schematic representation of the modeled tapered film is shown in Fig. 3.7. The film is modelled as a three-layered system, in which each layer represents an area of the film with homeotropic, planar or intermediate (45° tilt) alignments. The relative thickness of the layers is programmed according to the depths found with scanning electron microscopy (SEM), as seen in Fig. 3.4.

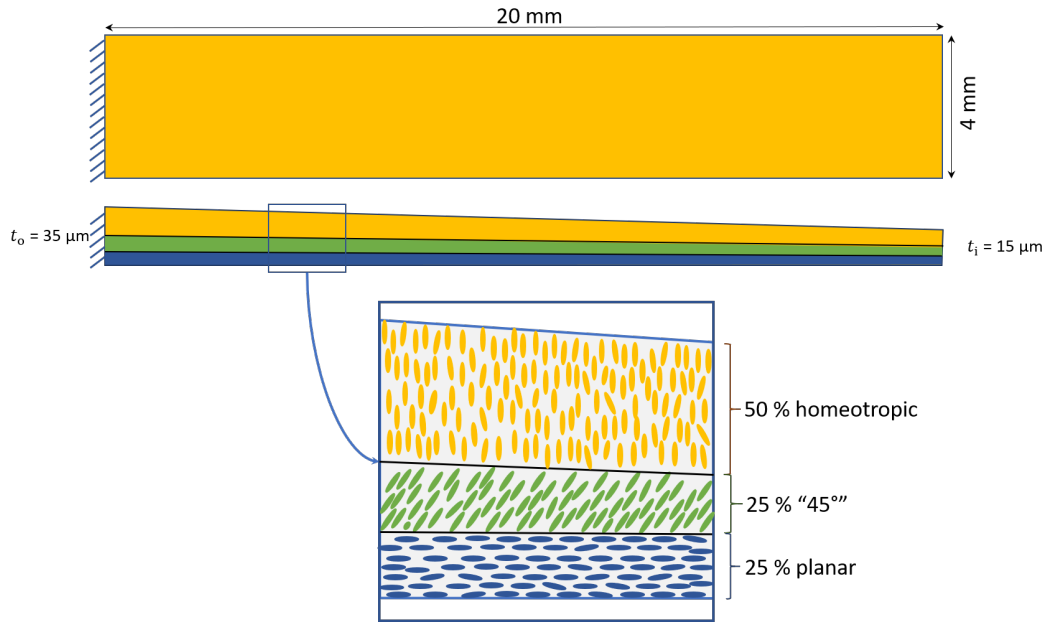


Figure 3.7: A schematic showing the geometric conditions and film alignment distribution along the thickness used in the finite element model.

There is a good correspondence between the predicted shapes and those achieved in practice (see Fig. 3.6), although the model somewhat over predicts the bending behaviour of the film above 65°C , the glass transition temperature. When plotting the inverse of the measured r_c (Fig. 3.8), juxtaposed with the finite element result for r_c , the same trend is seen even more clearly. We postulate that this is a result of a few factors. Firstly, the elastic moduli (E' and E'') of the material diminish strongly above T_g , decreasing at least an order of magnitude. However, as predicted by the model, the main

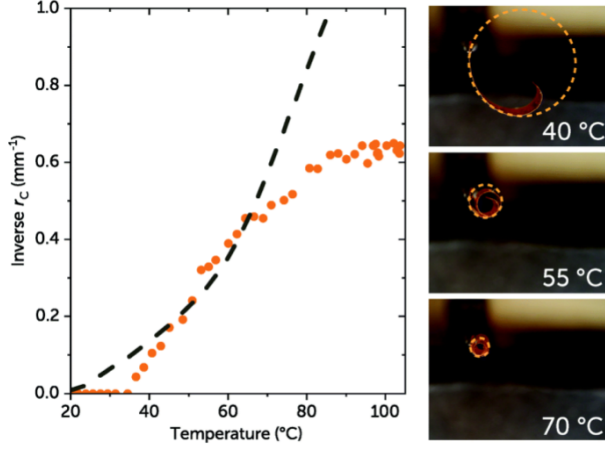


Figure 3.8: Plot showing measured r_c for the LCN film from Fig. 3.6 at different temperatures (orange circles). The dashed grey line is composed of r_c values from finite element analysis. Photographs on the right side detail the measurement method for r_c . [source: (Sol *et al.*, 2019)]

driver for rolling is the ratio between the elastic modulus parallel (E_{11}) and perpendicular (E_{22}, E_{33}) to \mathbf{n} . From DMA results (Fig. 3.3) it is seen that the ratio between these moduli is not significantly influenced by the glass transition. In contrast, self-contact by the film might lead to friction that hampers tighter rolling. This is especially relevant as the material has its T_g around 65 °C, above which it is soft, which could promote surface adhesion. We postulate that above T_g a combination of this surface adhesion phenomenon with the lower absolute values of the elastic moduli is responsible for the over prediction by the model. So far, modelling results have pointed out that the number of rotations made during thermal actuation depends mainly on the difference between thermal expansion coefficients ($\Delta\alpha$) parallel and perpendicular to \mathbf{n} (see Fig. 3.5 for data on thermal strain).

3.4 Summary

In summary, we have generated a series of LCN films from liquid crystalline networks that boast a tapered geometry, with one side of the film thinner than the other. Actuation triggered by heat results in a smooth transition from fully extended to extremely tightly rolled morphologies, which are completely reversible and reproducible. Generation of actuators using tapered LCN films could allow more dramatic and consistent motions, allowing their application over a much broader range of devices to come. Our suc-

cessful finite element predictive model allows a wide exploration of potential actuation mechanisms to identify promising candidates to be produced experimentally.

Chapter 4

Rock and roll motion of a thermo-responsive triangular LC film

Note: This chapter is partially reproduced from the authors' work submitted to Angwandte Chemie Int. Edition.

4.1 Introduction

Materials that undergo stimuli-triggered and self-powered oscillatory motion are extensively pursued for applications in medicine and soft robotics (Lu *et al.*, 2017; Rich *et al.*, 2018). Self-oscillating systems in nature, including the heartbeat, are a constant inspiration for the development of advanced stimuli-responsive materials (Merindol and Walther, 2017). Autonomous motions in polymers have been realized by utilizing variations in ambient humidity (Arazoe *et al.*, 2016), chemo-mechano-chemical effects (He *et al.*, 2012) and oscillating chemical reactions in gels such as the Belousov Zhabotinsky (BZ) reaction (Masuda *et al.*, 2013; Smith *et al.*, 2013; Zhou *et al.*, 2015). The continuous self-powered motion in polymers frees the devices from the dependence of on/off switching of external stimuli, and could dramatically expand the range of applications for the actuators, including in the areas of autonomous motors (Yamada *et al.*, 2008) and artificial muscles (Ikeda *et al.*, 2007). Self-powered motions in polymer actuators are often a result of feedback loops that couple material properties and external stimuli in synchronism.

The versatility of LCNs has allowed for the development of actuators capable of bending (Harris *et al.*, 2005; Kim *et al.*, 2015; Mol *et al.*, 2005; Sol *et al.*, 2019; Wani *et al.*, 2017), rolling (Wie *et al.*, 2016), ‘walking’ (Gelebart *et al.*, 2017a; Rogóz *et al.*, 2016) and helical twisting (Aßhoff *et al.*, 2017; Verpaalen *et al.*, 2018). Over the past few decades, light (Harris *et al.*, 2005; Van Oosten *et al.*, 2007), heat (Mol *et al.*, 2005) and humidity (de Haan *et al.*, 2014b) have been used as actuation triggers for these

responsive liquid crystalline networks. In LCNs, feedback loops arising from light-triggered deformation and self-shadowing have been exploited to generate oscillatory motion upon exposure to high intensity light (Ge *et al.*, 2018; Gelebart *et al.*, 2017b; Vantomme *et al.*, 2018; White *et al.*, 2008). In these latter systems, the LCN strip is clamped on one extremity while being exposed to a collimated light beam or a laser. The investigation of this self-powered motion has led to the design of continuous walkers/rollers powered upon exposure to light (Gelebart *et al.*, 2017a). Furthermore, continual oscillations in liquid crystal cantilevers have also been observed to be driven by sunlight (Kumar *et al.*, 2016). Even though the reported light triggered oscillations in LCN cantilevers are rooted in thermal deformations, solely thermally-fueled continuous motion is still undocumented for LCN actuators. Fully temperature triggered continuous actuation has been documented for a semi-crystalline random co-polymer upon exposure to a heated surface (Ge and Zhao, 2017). Through exposure to a surface of constant temperature, the material undergoes regional melting as a result of partial phase transitions. The mechanism for actuation is a thermo-mechano feedback loop which results in the self-powered motion of the material. More recently, a thermo-mechano electrical bilayer system was reported consisting of a three-dimensionally aligned ferroelectric polyvinylidene fluoride and polydopamine modified reduced graphene oxide-carbon nanotube layer capable of autonomous motion driven by heat (Bowen *et al.*, 2014).

In this work we present a monolayer, free-standing liquid crystal actuator demonstrating an unexpected continuous, self-powered oscillating motion initiated by contact with a heated surface as the only stimulus. We document geometry-specific motions for the polymer film, with triangular and parallelepiped shapes exhibiting unusual self-powered oscillations resembling a rocking chair, as the polymer film oscillates between two extreme states, rocking from tip to base in an irregular fashion, Fig. 4.1A. By the example of the triangular shaped film (see Fig. 4.1B) and through a finite element analysis, we propose the mechanism for the self-oscillation of the material with an insight into factors affecting the movement and suggest a feedback loop for the motion.

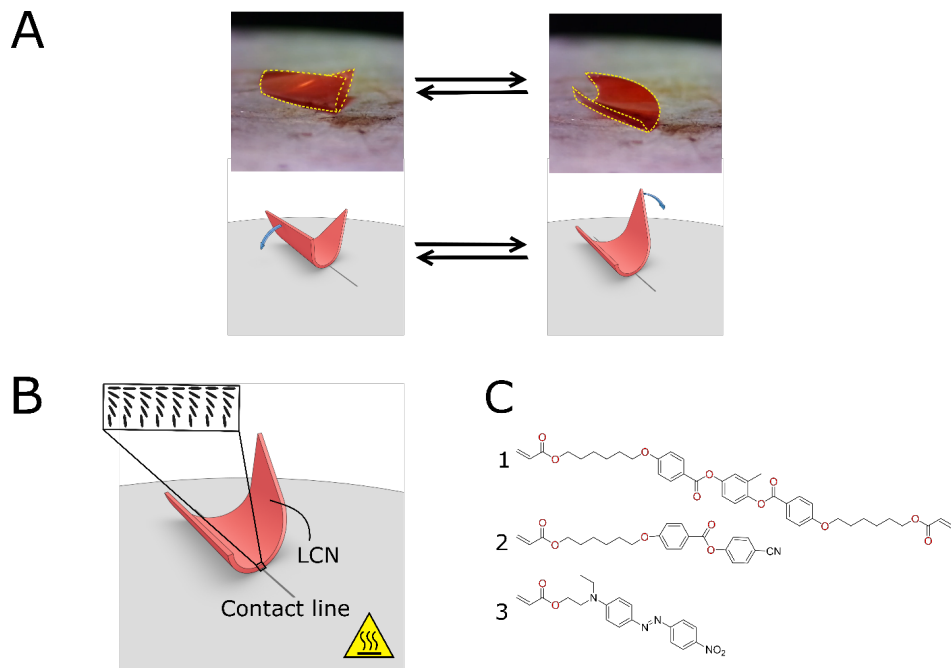


Figure 4.1: A) Snap-shots and schematic of the liquid crystal film during self-sustained motion on a heated surface. The snapshots depict the two extreme positions during oscillation. B) Schematic of the splay aligned LC film with equilateral triangular shape (sides of 30 mm) on a heated surface at 70°C; this position, in which the extremities of the film are raised above the heated surface and a contact line (dotted blue line) is established between the LCN and the surface, and is the initial deformation prior to the initiation of rocking motion. C) Chemical structures of monomers (1, 2) in the liquid crystal polymeric network with splay molecular alignment and the active azobenzene derivative (3). (Courtesy: Marina Pilz da Cunha, TU Eindhoven, The Netherlands)

4.2 Synthesis and characterization of LCN films

The liquid crystal polymer network is produced by the photo-copolymerization of two liquid crystalline monomers (Fig. 4.1C): a monoacrylate, 2, (RM 23; 40,5mol%, Merck) and a diacrylate, 1, (RM82; 56,5mol%, Merck), initiated by a photoinitiator (Irgacure 819, 1mol%, Ciba). Prior to polymerization, the monomers were dissolved in dichloro methane to obtain a homogeneous mixture; the solvent was subsequently evaporated. Custom-made cells were prepared by gluing together two glass slides coated with differing polyimide alignment layers (for a splay alignment one slide with planar and the other with homeotropic alignment layers (Optimer AL 1051 (JSR Micro) and 5661 polyimide (Sunever), respectively)) with 20 µm diameter glass bead spacers incorporated into the glue to achieve controlled cell thickness. The cells were filled at 95 °C, at which the LC mixture is isotropic through capillary action. Subsequently, the filled

cell was cooled to 80 °C, at which temperature the LC mixture is nematic. Photopolymerization of the reactive mesogens was done at 80 °C with an Exfo Omnicure S2000 lamp; subsequent thermal treatment at 120 °C for 10 minutes released thermal stresses arising from polymer shrinkage during polymerization. After polymerization, the cell was opened, and the films are peeled from the glass with razor blades and cut into the required shapes. The films showed similar characteristics as the films presented in Chapter 3. The thermal expansion coefficient of the films for different strain directions is measured and presented in Fig. 4.2.

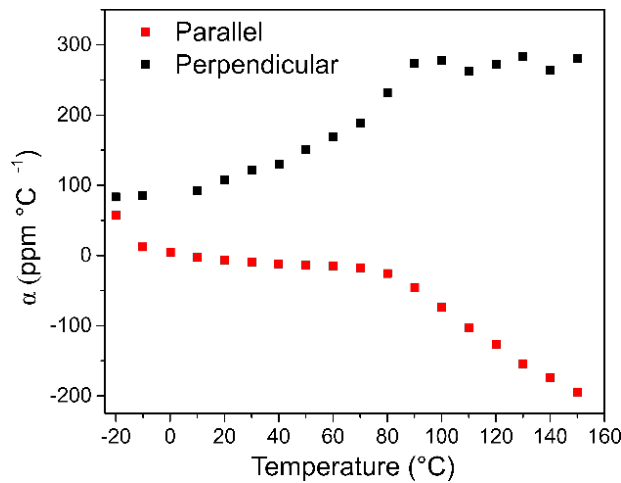


Figure 4.2: Coefficients of thermal expansion, perpendicular (black squares) and parallel (red squares) to the molecular orientation director \mathbf{n} measured with reference temperature as -20 °C. (Courtesy: Marina Pilz da Cunha, TU Eindhoven, The Netherlands)

4.3 Self-sustained Rocking

The anisotropic shape of liquid crystalline molecules can be utilized to create macroscopic deformations in polymer films through controlled molecular alignments. Anisotropic alignments such as splay and twisted nematic, in which the molecular alignment is varied through the network's thickness, have been shown to result in large temperature-triggered deformations in LCNs due to additive effects of thermal expansion of opposing surfaces of the film (Mol *et al.*, 2005). For the actuator presented here, a self-assembling, splay aligned LCN is used wherein on one side of the film the molecules are aligned parallel to the surface and on the other perpendicular (planar and homeotropic alignment, respectively). The polymer film is polymerized at an elevated temperature (80 °C), giving it a pre-bent shape at room temperature due to increased molecular or-

der at lower temperature: upon cooling to room temperature from the more disordered state, the molecular order increase leads to anisotropic molar volume shrinkage, with contraction perpendicular to the molecular director and expansion parallel to the director; this causes the homeotropic side of the splay to be on the inside of the film's pre-bent shape.

Curiously, we observe a thermally fueled oscillatory motion when an equilateral triangle splay film is placed with its homeotropic surface in contact with a hot plate set between 70-80 °C. Upon contact with the heated surface, the film's extremities are lifted off the heated surface, creating a curved geometry in which a localized contact line is established between the film and the hot plate, Fig. 4.1B. Subsequently, a rapid back-and-forth rocking motion commences and is sustained for multiple cycles. Further increasing the temperature to the material's glass transition temperature (83 °C) stops the continual motion as the material starts to undergo plastic deformation. No rocking motion is observed when the heated surface is below 70 °C or when the triangular film is placed with its planar side contacting the hot plate.

More information on the nature of thermally induced oscillations is obtained by tracking the displacement of one of the film's extremities in time. Tracking of the triangular film's tip displacement when the film initiates oscillatory motion, (Fig. 4.3) shows that the rocking motion does not follow an obvious harmonic motion; instead it displays an apparent semi-random displacement. During rocking motion, the film oscillates from two extreme positions and the triangular shape shows different degrees of curvature at each extreme. Irregularities in the displacement are more commonly observed during the reverse motion. The forward motion, from point i to ii in Fig. 4.3B, is more consistent with an average tip speed of 7.2 cm/s ($\pm 17\%$).

Furthermore, we have observed that the geometry of the LCN film is important for the oscillatory motion to be sustained. A rectangular or square splay film of the same composition deforms similarly to the triangular film upon initial contact of the homeotropic surface with the hot plate, with the edges lifted off the surface and the establishment of a contact line. However, the subsequent deformation results in a toppling of the film onto the planar surface. This state will not initiate further motions and the film remains nearly flat on the surface. We propose that one of the requirements for oscillation to commence is that after establishment of the contact line between the

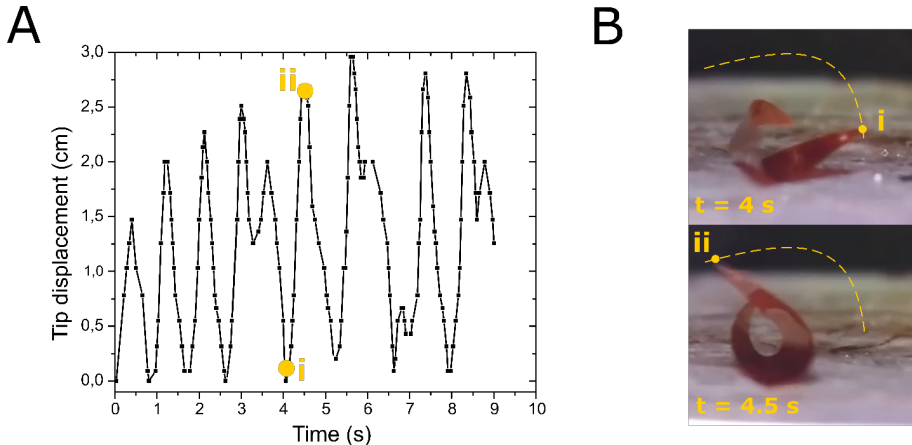


Figure 4.3: A) Plot tracking triangle's tip displacement after the film has initiated oscillatory motion. The tip's path follows the dashed yellow line in the snapshot in 4.3B, with points i and ii showing the two displacement extremes during an oscillation cycle. B) Snapshots of one actuation cycle in which the tip moves away from the heated surface following a curved path, (i - ii); the hot plate temperature is set to 72 °C. (Courtesy: Marina Pilz da Cunha, TU Eindhoven, The Netherlands)

film and the heated surface, the geometry of the raised extremities cannot be mirror images of each other, as is the case for a rectangular/square film. Despite the similar geometry to a rectangle, a parallelepiped (with similar dimensions), does not show immediate toppling but displays oscillatory motion similar to the triangular shape. For a parallelepiped, comparison across the contact line does not present a mirror image of the raised extremities and we believe this condition prevents immediate toppling of the film and results in rocking motion.

The self-powered oscillatory motion of shape-specific LCNs is rooted in both the temperature-triggered shape deformations and in a steep thermal gradient between the contact line of the film with the hot plate and its raised extremities. Elucidation of the mechanism driving the rocking motion requires a detailed understanding of the temperature driven deformations of the LCN. As mentioned previously, due to the opposing alignment directions of the two film surfaces, anisotropic thermal expansion leads to thermally driven deformations with three main deformation shapes: below, at, and above T_f , (see Fig. 4.4A). Upon heating of the polymer network, one side displays volumetric expansion parallel to the surface (homeotropic side), and the other anisotropic contraction (planar side), resulting in macroscopic bending deformation. At room temperature the network has a bent shape, with the homeotropic side of the splay on the inside of the curl, and upon heating the network, the film extends to a flat shape (ob-

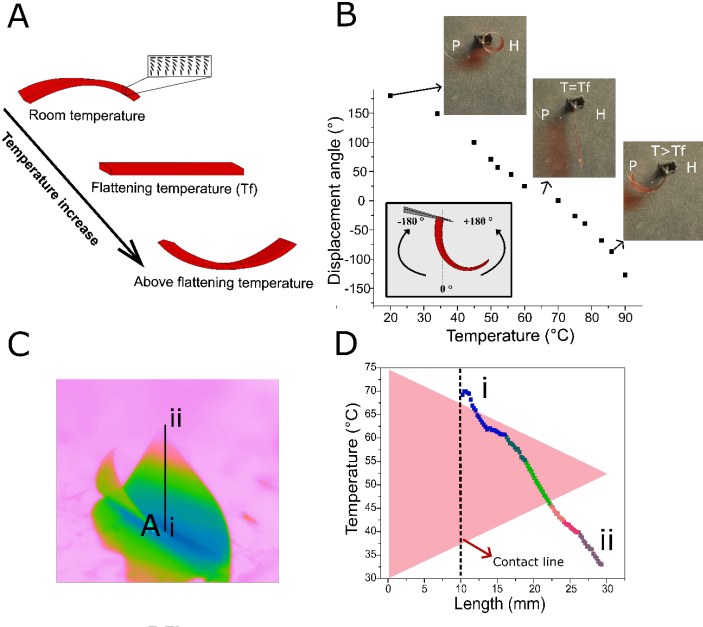


Figure 4.4: A) Schematic drawing of the temperature triggered deformation of a splay aligned LCN strip with three main deformation shapes: below, at, and above T_f . B) Deformation plot for the LC film (1.6 cm in length) in response to temperature variation in an oven. ‘P’ and ‘H’ refer to the planar and homeotropic sides of the splay film, respectively. C) Thermal image of the triangular film in contact with a heated surface above T_f , showing a steep thermal gradient along the film’s length. D) Plot showing the thermal gradient along the length of the triangular film (Line A in Fig. 4.4C, the colors of the data corresponding to the colors in the thermal photograph). (Courtesy: Marina Pilz da Cunha, TU Eindhoven, The Netherlands)

served at 60–65 °C), followed by bending in the opposite direction, with the planar side now on the inside the curl (see Fig. 4.4B). Thermal actuation in an oven from room temperature to 90°C is reversible for several cycles. Thermal imaging reveals that while the triangular film undergoes oscillatory motion on a hot plate, tipping from tip to base, steep thermal gradients are present along the film’s length (see Fig. 4.4C). The temperature variations follow a linear decrease with increasing distance from the contact line, going from 70 °C at the contact line to 33 °C at the tip’s extremity as shown in Fig. 4.4D.

To gain insight into the mechanism driving the self-sustained oscillations, a finite element model was developed. We model the LCN as a three-layered system, with individual layers as different alignment domains: homeotropic, intermediate (45° tilt) and planar. The simulations incorporate the temperature response of the network as well as a temperature distribution along the length of the films. In the modelled system, we apply a piece-wise linear distribution of the temperature variation as a function of the

position of the contact line between the film and the heated surface. Simulations show triangular films to undergo chaotic oscillatory motion with similar tip displacement amplitudes (see Fig. 4.5A) to experimental observations (see Fig. 4.3).

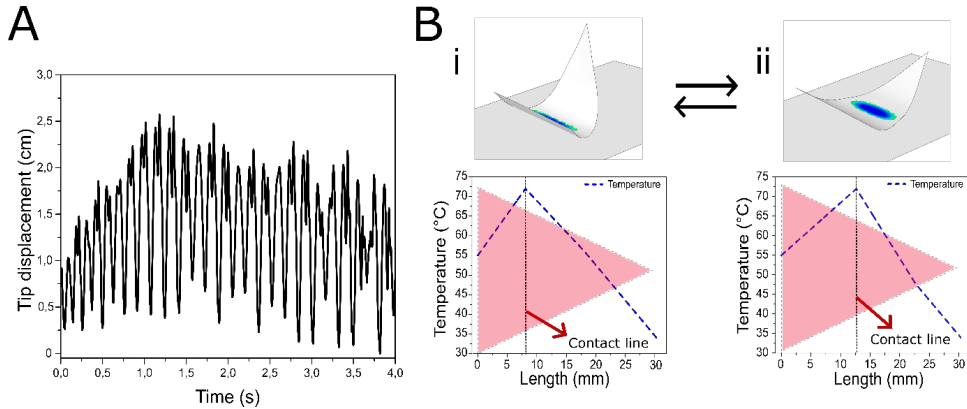


Figure 4.5: A) Plot resultant from tracking the triangular film's tip displacement obtained from the finite element simulation during multiple oscillation cycles. B) The two depicted positions of the film, i and ii, represent the two displacement extremes during rocking, as shown in Figure 2B. The plots demonstrate the corresponding temperature profile arising through the length of the film (blue dashed line) based on the position of the contact line.

Simulations demonstrate that the location of the contact line rapidly changes during rocking motion, with variation between situation depicted in Figs. 4.5B i and 4.5B ii being the timescale of one oscillation. Additionally, we observe that at different stages of the rocking motion, the effective thermal gradient over the film's length varies with shifting location of the contact line, Fig. 4.5. Zones near the contact line experience large variations in temperature, causing localized thermal strain. Localized cooling in regions becoming distal to the now-shifted contact line leads to strain relaxation in these locations. The variation in temperature and relaxation of thermal strain, primarily in the immediate vicinity of the contact line (note the minimal changes of the tip temperatures during the rocking), leads to different degrees of bending as a function of local temperature (Fig. 4.4A, *vide supra*), unbalancing the bent triangular film and shifting the film's center of gravity. The shifting center of gravity, fueled by local deformation and the location of the contact line results in rocking between two unstable states, i and ii Fig. 4.5B.

Experimentally, we observe that even asymmetric shapes occasionally undergo toppling motion. The toppling motion follows an oscillation with unusually high amplitude. It is likely that a threshold value for oscillation amplitudes (A_t) exists, which

when surpassed causes the film to undergo toppling. The magnitude of the threshold amplitude depends on shape asymmetry; a higher degree of asymmetry shows higher A_t values, allowing for higher amplitude of rocking without toppling. We have simulated a triangle that experiences an oscillation amplitude exceeding A_t , and it exhibits a toppling motion similar to objects with lower degrees of asymmetry, such as rectangles or squares. We propose that for self-sustained oscillations to be maintained, the system must display a unique interplay between shape asymmetry and temperature profile over the length of film, primarily intimate to the contact region.

A step-wise schematic of mechanical deformations leading to the feedback loop for the sustained oscillations is depicted in Fig. 4.6. As formerly described, and additionally depicted here by step i and ii in Fig. 4.6, when the film is placed with the homeotropic surface in contact with the hot plate heated above T_f , it adopts a curled shape, with opposite concavity to its preliminary, pre-bent shape at room temperature. This curling causes the extreme edges of the film to lift from the heated surface, and a localized contact region between the film and hot plate is established, Fig. 4.6 ii, creating a thermal gradient along the length of the raised section. Upon cooling, these regions experience strain relaxation and change their degree of bending, unbalancing the structure causing tipping towards one side, Fig. 4.6 iii. Consequently, this changes the contact line between the film and hot plate, causing a variation in the thermal gradient, Fig. 4.6 iv, causing immediate local heating in this new contact area. Consequently, the area previously heated now cools, Fig. 4.6 v, and undergoes an identical sequence of bending events, setting in motion the self-powered feedback loop through Fig. 4.6 iii - vi.

4.4 Summary

In summary, we disclose a novel, continuous rocking motion of a liquid crystal network initiated and sustained simply by a constant heat source located below the device. Via a combination of local actuation, geometric shape, and thermal gradients, various bending directions are found within proximity in the same film, resulting in continual imbalance in the structure, and manifested as a self-sustained rocking motion. The finite element simulations show that the sustained oscillations are geometry dependent

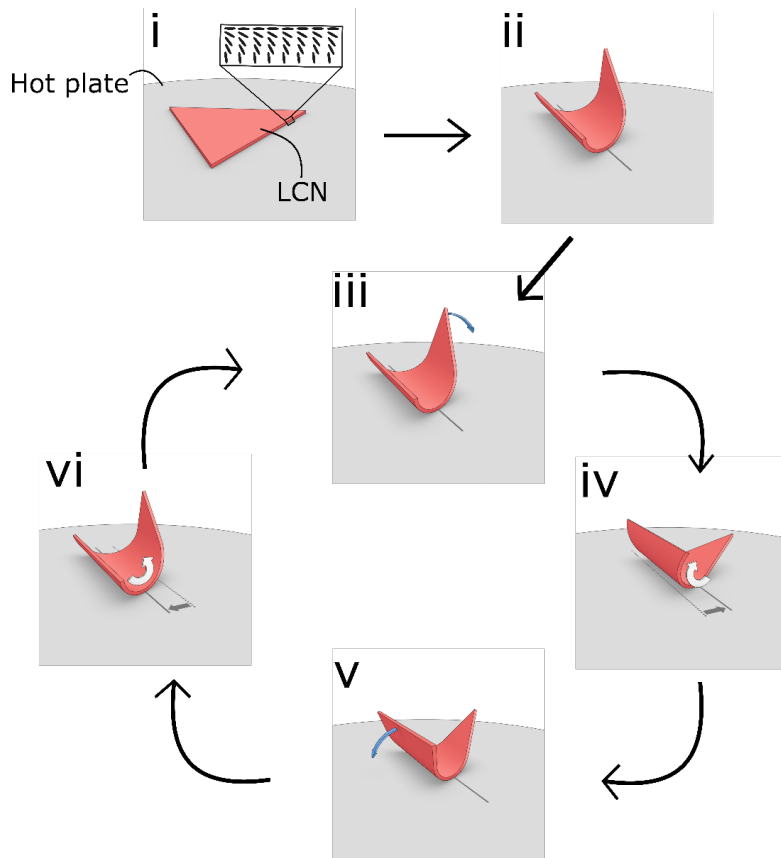


Figure 4.6: Schematic of the mechanism for the self-sustained feedback loop for the triangular LCN upon contact of its homeotropic side with a heated surface at constant temperature. Highlighted in blue are the areas that undergo bending deformation towards the heated surface, leading to a shift in the film's center of gravity. (Courtesy: Marina Pilz da Cunha, TU Eindhoven, The Netherlands)

and that temperature specific deformations propel the oscillatory motion.

Chapter 5

Summary and Future Scope

In summary, a methodology to implement the varying spatial orientation of liquid crystal thin films in the commercial finite element software ABAQUS is developed. The developed finite element model is then validated by comparing with the finite element results with the Timoshenko's analytical result for a bi-layer film. The developed methodology is then used to generate insights into the design of soft-actuators - by designing the alignment distribution, boundary conditions and shape of the initial film to generate rolls from rectangular thin films. The designed tapered thin film is fabricated experimentally by our collaborators. The simulation results corroborate well with the experimental results. The tapered rectangular thin film showed almost 4 rolls in comparison with the only 1-2 rolls for different film designs presented in the literature. By playing with the geometries and alignment distributions, different shapes can be generated. One such extension from a rolling tapered film is the transformation of a planar quarter circle or square film into a cone. With the tapering and planar alignment along the 45° from the edges (see Fig. 5.1) and splayed alignment distribution, the plane film deforms into cones as shown in Figures 5.2 and 5.3. Generation of soft-actuators using proposed tapered LCN films could allow even more complex and reproducible motions, allowing their application over a much broader range of devices to come.

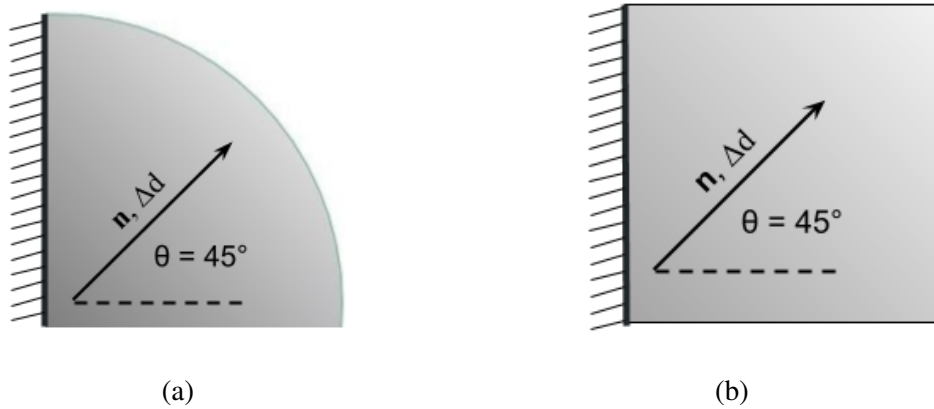


Figure 5.1: Alignment and tapering direction for the a) quarter circle and b) square film needed to generate cones.

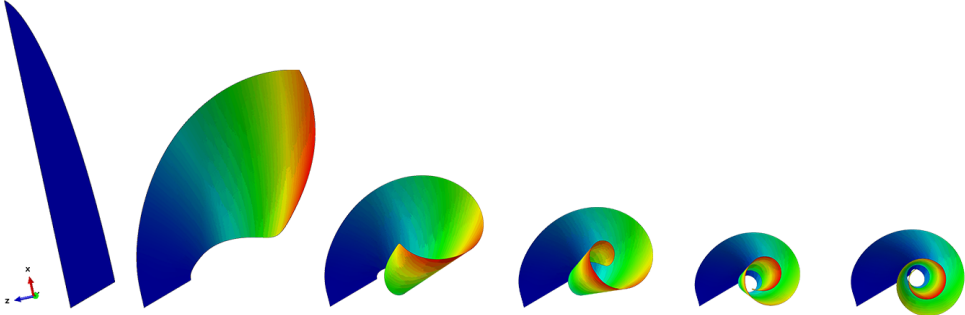


Figure 5.2: Finite element simulation of a cone formation from a quarter circular tapered LCN film.

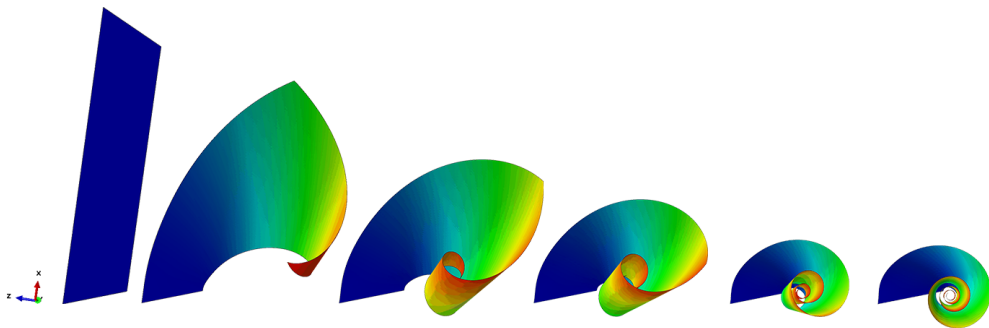


Figure 5.3: Finite element simulation of a cone formation from a Square diagonally tapered LCN film.

The model is also extended to simulate the self-sustained rocking motion observed when a triangular liquid crystal thin film comes in contact with a hot plate. Through finite element simulations, we have shown that the sustained oscillations are geometry dependent and that temperature specific deformations propel the oscillatory motion. A hypothesis is proposed for the observed rocking in asymmetrical films and toppling in approximately symmetric films based on the understanding developed from the simulations. The computational modeling can be further improved by performing the heat transfer simulations of the film at each increment rather than specifying the temperature distribution directly. The thermo-mechanical feedback present in the self-sustained rocking of thin films can be used to develop to and fro motion in wheels. As discussed above the geometry plays a major role in creating the rocking motion. To create such a periodic motion, the wheel should be made from a tapered rectangular film by joining the thicker and thinner ends as schematically visualized in Fig. 5.4. Such a film on contact with the hot plate can show the periodic motion between two points separated by the length of the initial film as a result of the interplay between heating, cooling and the gravity. The periodic motion of this kind can be achieved as shown in Fig. 5.5 (forward

motion) and Fig. 5.6 (backward motion).

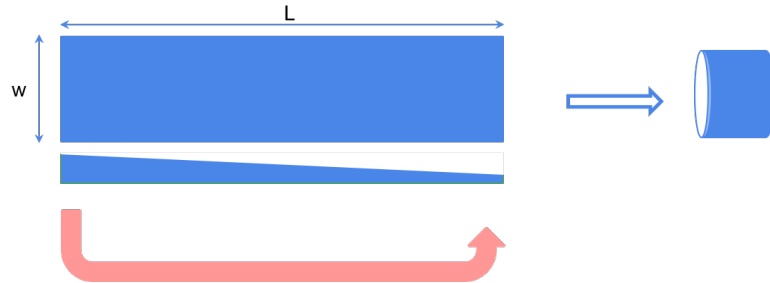


Figure 5.4: Schematic representation of formation of a wheel from a tapered rectangular LCN film

To conclude, the philosophy of simulation assisted experiments is followed in this project creating never before seen shapes and motions in thermal-responsive liquid crystal thin films. The developed finite element predictive model allows for a wide exploration of possible actuation mechanisms for recognizing promising candidates to be produced experimentally. Furthermore, the same methodology can be extended to liquid crystal thin films responsive to other sources of stimuli such as light and humidity.

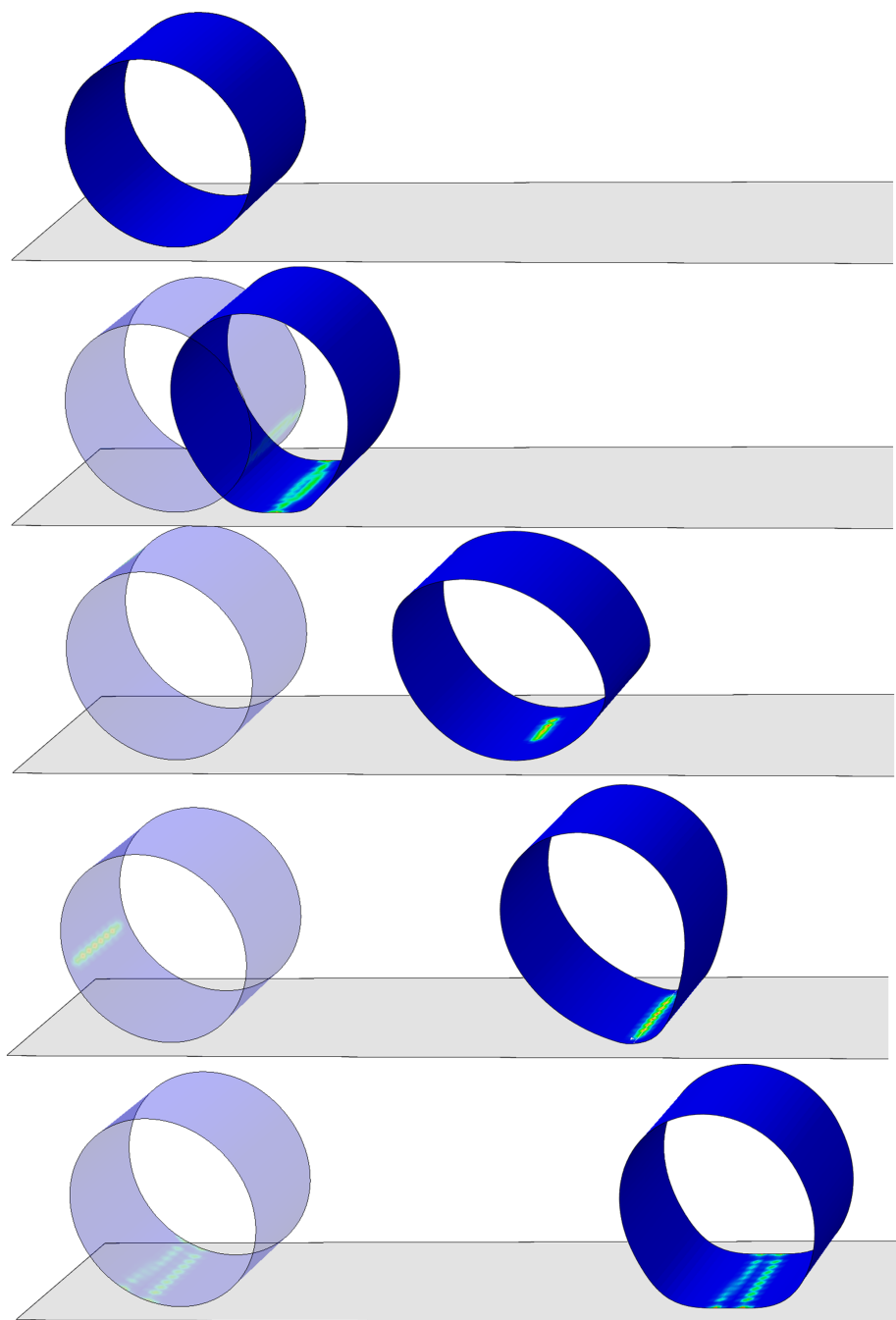


Figure 5.5: Forward motion of wheel made of tapered LCN film

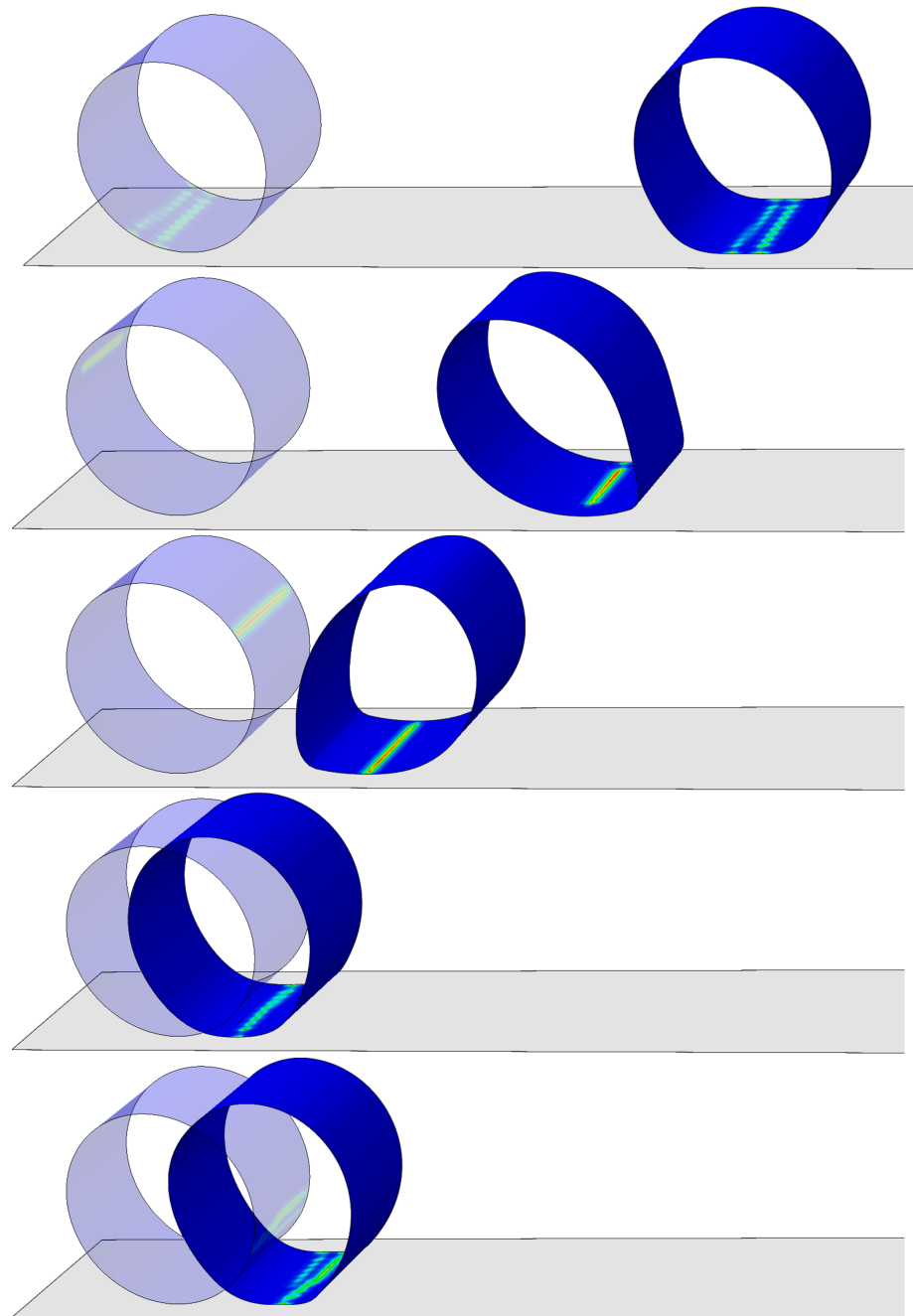


Figure 5.6: Backward motion of wheel made of tapered LCN film

Bibliography

1. **Arazoe, H., D. Miyajima, K. Akaike, F. Araoka, E. Sato, T. Hikima, M. Kawamoto, and T. Aida** (2016). An autonomous actuator driven by fluctuations in ambient humidity. *Nature materials*, **15**(10), 1084.
2. **Aßhoff, S. J., F. Lancia, S. Iamsaard, B. Matt, T. Kudernac, S. P. Fletcher, and N. Katsonis** (2017). High-Power Actuation from Molecular Photoswitches in Enantiomerically Paired Soft Springs. *Angewandte Chemie International Edition*, **56**(12), 3261–3265. ISSN 14337851.
3. **Bai, F., J. Wu, G. Gong, and L. Guo** (2014). Biomimetic “water strider leg” with highly refined nanogroove structure and remarkable water-repellent performance. *ACS applied materials & interfaces*, **6**(18), 16237–16242.
4. **Bowen, C. R., J. Taylor, E. LeBoulbar, D. Zabek, A. Chauhan, and R. Vaish** (2014). Pyroelectric materials and devices for energy harvesting applications. *Energy & Environmental Science*, **7**(12), 3836–3856.
5. **Broer, D., G. P. Crawford, and S. Zumer**, *Cross-linked liquid crystalline systems: from rigid polymer networks to elastomers*. CRC press, 2011.
6. **Cianchetti, M., C. Laschi, A. Menciassi, and P. Dario** (2018). Biomedical applications of soft robotics. *Nature Reviews Materials*, **3**(6), 143–153. ISSN 2058-8437.
7. **de Haan, L. T., V. Gimenez-Pinto, A. Konya, T.-S. Nguyen, J. M. N. Verjans, C. Sánchez-Somolinos, J. V. Selinger, R. L. B. Selinger, D. J. Broer, and A. P. H. J. Schenning** (2014a). Accordion-like actuators of multiple 3D patterned liquid crystal polymer films. *Advanced Functional Materials*, **24**(9), 1251–1258.
8. **de Haan, L. T., J. M. Verjans, D. J. Broer, C. W. Bastiaansen, and A. P. Schenning** (2014b). Humidity-responsive liquid crystalline polymer actuators with an asymmetry in the molecular trigger that bend, fold, and curl. *Journal of the American Chemical Society*, **136**(30), 10585–10588.
9. **Ganta, S., H. Devalapally, A. Shahiwala, and M. Amiji** (2008). A review of stimuli-responsive nanocarriers for drug and gene delivery. *Journal of controlled release*, **126**(3), 187–204.
10. **Ge, F., R. Yang, X. Tong, F. Camerel, and Y. Zhao** (2018). A multifunctional dye-doped liquid crystal polymer actuator: Light-guided transportation, turning in locomotion, and autonomous motion. *Angewandte Chemie International Edition*, **57**(36), 11758–11763.
11. **Ge, F. and Y. Zhao** (2017). A new function for thermal phase transition-based polymer actuators: autonomous motion on a surface of constant temperature. *Chemical science*, **8**(9), 6307–6312.

12. **Gelebart, A. H., D. Jan Mulder, M. Varga, A. Konya, G. Vantomme, E. W. Meijer, R. L. B. Selinger, and D. J. Broer** (2017a). Making waves in a photoactive polymer film. *Nature*, **546**(7660), 632–636. ISSN 0028-0836.
13. **Gelebart, A. H., G. Vantomme, E. Meijer, and D. J. Broer** (2017b). Mastering the photothermal effect in liquid crystal networks: a general approach for self-sustained mechanical oscillators. *Advanced Materials*, **29**(18), 1606712.
14. **Harris, K. D., R. Cuypers, P. Scheibe, C. L. van Oosten, C. W. M. Bastiaansen, J. Lub, and D. J. Broer** (2005). Large amplitude light-induced motion in high elastic modulus polymer actuators. *Journal of Materials Chemistry*, **15**(47), 5043–5048.
15. **He, X., M. Aizenberg, O. Kuksenok, L. D. Zarzar, A. Shastri, A. C. Balazs, and J. Aizenberg** (2012). Synthetic homeostatic materials with chemo-mechano-chemical self-regulation. *Nature*, **487**(7406), 214.
16. **Ikeda, T., J.-i. Mamiya, and Y. Yu** (2007). Photomechanics of liquid-crystalline elastomers and other polymers. *Angewandte Chemie International Edition*, **46**(4), 506–528.
17. **Kim, K. H., T. Umakoshi, Y. Abe, M. Kawamura, and T. Kiba** (2015). Determination of effective growth time for zinc oxide nanorods using chemical solution deposition. *Superlattices and Microstructures*, **88**, 150–153.
18. **Krenn, H. W.** (2010). Feeding mechanisms of adult lepidoptera: structure, function, and evolution of the mouthparts. *Annual review of entomology*, **55**, 307–327.
19. **Krenn, H. W. and N. P. Kristensen** (2004). Evolution of proboscis musculature in lepidoptera. *European Journal of Entomology*, **101**(4), 565.
20. **Krenn, H. W. and N. Mühlberger** (2002). Groundplan anatomy of the proboscis of butterflies (papilioidea, lepidoptera). *Zoologischer Anzeiger-A Journal of Comparative Zoology*, **241**(4), 369–380.
21. **Kumar, K., C. Knie, D. Bléger, M. A. Peletier, H. Friedrich, S. Hecht, D. J. Broer, M. G. Debije, and A. P. Schenning** (2016). A chaotic self-oscillating sunlight-driven polymer actuator. *Nature communications*, **7**, 11975.
22. **Lahikainen, M., H. Zeng, and A. Priimagi** (2018). Reconfigurable photoactuator through synergistic use of photochemical and photothermal effects. *Nature Communications*, **9**(1), 4148. ISSN 2041-1723.
23. **Liu, D. and D. J. Broer** (2014). Liquid crystal polymer networks: preparation, properties, and applications of films with patterned molecular alignment. *Langmuir*, **30**(45), 13499–13509.
24. **Liu, D. and D. J. Broer**, *Responsive polymer surfaces: dynamics in surface topography*. John Wiley & Sons, 2017.
25. **Liu, L. and P. R. Onck** (2018). Topographical changes in photo-responsive liquid crystal films: a computational analysis. *Soft matter*, **14**(12), 2411–2428.
26. **Lu, X., S. Guo, X. Tong, H. Xia, and Y. Zhao** (2017). Tunable photocontrolled motions using stored strain energy in malleable azobenzene liquid crystalline polymer actuators. *Advanced Materials*, **29**(28), 1606467.

27. **Masuda, T., M. Hidaka, Y. Murase, A. M. Akimoto, K. Nagase, T. Okano, and R. Yoshida** (2013). Self-oscillating polymer brushes. *Angewandte Chemie International Edition*, **52**(29), 7468–7471.
28. **McConney, M. E., A. Martinez, V. P. Tondiglia, K. M. Lee, D. Langley, I. I. Smalyukh, and T. J. White** (2013). Topography from topology: photoinduced surface features generated in liquid crystal polymer networks. *Advanced Materials*, **25**(41), 5880–5885.
29. **Meng, H. and G. Li** (2013). A review of stimuli-responsive shape memory polymer composites. *Polymer*, **54**(9), 2199–2221.
30. **Merindol, R. and A. Walther** (2017). Materials learning from life: concepts for active, adaptive and autonomous molecular systems. *Chemical Society Reviews*, **46**(18), 5588–5619.
31. **Mol, G. N., K. D. Harris, C. W. M. Bastiaansen, and D. J. Broer** (2005). Thermo-Mechanical Responses of Liquid-Crystal Networks with a Splayed Molecular Organization. *Advanced Functional Materials*, **15**(7), 1155–1159. ISSN 1616-301X.
32. **Nocentini, S., D. Martella, D. Nuzhdin, C. Parmeggiani, and D. S. Wiersma**, Photonic arms, legs, and skin. In *Optical Trapping and Optical Micromanipulation XIV*, volume 10347. International Society for Optics and Photonics, 2017.
33. **Palagi, S. and P. Fischer** (2018). Bioinspired microrobots. *Nature Reviews Materials*, **1**.
34. **Pei, Z., Y. Yang, Q. Chen, E. M. Terentjev, Y. Wei, and Y. Ji** (2014). Mouldable liquid-crystalline elastomer actuators with exchangeable covalent bonds. *Nature Materials*, **13**(1), 36.
35. **Rich, S. I., R. J. Wood, and C. Majidi** (2018). Untethered soft robotics. *Nature Electronics*, **1**(2), 102.
36. **Rogóz, M., H. Zeng, C. Xuan, D. S. Wiersma, and P. Wasylczyk** (2016). Light-driven soft robot mimics caterpillar locomotion in natural scale. *Advanced Optical Materials*, **4**(11), 1689–1694.
37. **Ryu, J., M. D'Amato, X. Cui, K. N. Long, H. Jerry Qi, and M. L. Dunn** (2012). Photo-origami - Bending and folding polymers with light. *Applied Physics Letters*, **100**(16), 161908.
38. **Smith, M.**, *ABAQUS/Standard User's Manual, Version 6.9*. Simulia, 2009.
39. **Smith, M. L., C. Slone, K. Heitfeld, and R. A. Vaia** (2013). Designed autonomic motion in heterogeneous belousov–zhabotinsky (bz)-gelatin composites by synchronicity. *Advanced Functional Materials*, **23**(22), 2835–2842.
40. **Sol, J., A. Peeketi, N. Vyas, A. Schenning, R. Annabattula, and M. Debie** (2019). Butterfly proboscis-inspired tight rolling tapered soft actuators. *Chemical Communications*, **55**(12), 1726–1729.
41. **Timoshenko, S.** (1925). Analysis of Bi-Metal Thermostats. *Journal of the Optical Society of America*, **11**(3), 233. ISSN 0030-3941.

42. **van Oosten, C. L., C. W. M. Bastiaansen, and D. J. Broer** (2009). Printed artificial cilia from liquid-crystal network actuators modularly driven by light. *Nature Materials*, **8**(8), 677–682. ISSN 1476-1122.
43. **Van Oosten, C. L., K. D. Harris, C. W. M. Bastiaansen, and D. J. Broer** (2007). Glassy photomechanical liquid-crystal network actuators for microscale devices. *The European Physical Journal E*, **23**(3), 329–336.
44. **Vantomme, G., A. H. Gelebart, D. J. Broer, and E. Meijer** (2018). Self-sustained actuation from heat dissipation in liquid crystal polymer networks. *Journal of Polymer Science Part A: Polymer Chemistry*, **56**(13), 1331–1336.
45. **Verpaalen, R. C., M. G. Debije, C. W. Bastiaansen, H. Halilović, T. A. Engels, and A. P. Schenning** (2018). Programmable helical twisting in oriented humidity-responsive bilayer films generated by spray-coating of a chiral nematic liquid crystal. *Journal of Materials Chemistry A*, **6**(36), 17724–17729.
46. **Visschers, F. L., M. Hendrikx, Y. Zhan, and D. Liu** (2018). Liquid crystal polymers with motile surfaces. *Soft matter*, **14**(24), 4898–4912.
47. **Wallin, T. J., J. Pikul, and R. F. Shepherd** (2018). 3D printing of soft robotic systems. *Nature Reviews Materials*, **3**(6), 84–100. ISSN 2058-8437.
48. **Wani, O. M., H. Zeng, and A. Priimagi** (2017). A light-driven artificial flytrap. *Nature Communications*, **8**, 15546. ISSN 2041-1723.
49. **Ware, T. H., M. E. McConney, J. J. Wie, V. P. Tondiglia, and T. J. White** (2015). Voxelated liquid crystal elastomers. *Science*, **347**(6225), 982–984.
50. **Warner, M., C. D. Modes, and D. Corbett** (2010). Curvature in nematic elastica responding to light and heat. *Proceedings of the Royal Society of London A: Mathematical, Physical and Engineering Sciences*, **466**(2122), 2975–2989.
51. **Wei, M., Y. Gao, X. Li, and M. J. Serpe** (2017). Stimuli-responsive polymers and their applications. *Polymer Chemistry*, **8**(1), 127–143.
52. **White, T. J., Photomechanical Materials, Composites, and Systems: Wireless Transduction of Light into Work**. John Wiley & Sons, 2017.
53. **White, T. J. and D. J. Broer** (2015). Programmable and adaptive mechanics with liquid crystal polymer networks and elastomers. *Nature Materials*, **14**(11), 1087.
54. **White, T. J., N. V. Tabiryan, S. V. Serak, U. A. Hrozyk, V. P. Tondiglia, H. Koerner, R. A. Vaia, and T. J. Bunning** (2008). A high frequency photodriven polymer oscillator. *Soft Matter*, **4**(9), 1796–1798.
55. **Wie, J. J., M. R. Shankar, and T. J. White** (2016). Photomotility of polymers. *Nature communications*, **7**, 13260.
56. **Woltman, S. J., G. D. Jay, and G. P. Crawford** (2007). Liquid-crystal materials find a new order in biomedical applications. *Nature Materials*, **6**(12), 929.
57. **Yamada, M., M. Kondo, J.-i. Mamiya, Y. Yu, M. Kinoshita, C. J. Barrett, and T. Ikeda** (2008). Photomobile polymer materials: towards light-driven plastic motors. *Angewandte Chemie International Edition*, **47**(27), 4986–4988.

58. **Zeng, H., O. M. Wani, P. Wasylczyk, and A. Priimagi** (2018a). Light-Driven, Caterpillar-Inspired Miniature Inchworm Robot. *Macromolecular Rapid Communications*, **39**(1), 1700224. ISSN 10221336.
59. **Zeng, H., P. Wasylczyk, C. Parmeggiani, D. Martella, M. Burresi, and D. S. Wiersma** (2015). Light-Fueled Microscopic Walkers. *Advanced Materials*, **27**(26), 3883–3887. ISSN 09359648.
60. **Zeng, H., P. Wasylczyk, D. S. Wiersma, and A. Priimagi** (2018b). Light Robots: Bridging the Gap between Microrobotics and Photomechanics in Soft Materials. *Advanced Materials*, **30**(24), 1703554. ISSN 09359648.
61. **Zhou, H., Z. Zheng, Q. Wang, G. Xu, J. Li, and X. Ding** (2015). A modular approach to self-oscillating polymer systems driven by the belousov–zhabotinsky reaction. *RSC Advances*, **5**(18), 13555–13569.
62. **Ziółkowski, B., M. Czugala, and D. Diamond** (2013). Integrating stimulus responsive materials and microfluidics: The key to next-generation chemical sensors. *Journal of Intelligent Material Systems and Structures*, **24**(18), 2221–2238.

LIST OF PAPERS BASED ON THE PROJECT

1. Jeroen A. H. P. Sol, **Akhil R Peeketi**, Nihit Vyas, Albertus P. H. J. Schenning, Ratna K Annabattula, Michael G. Debije. Butterfly proboscis-inspired tight rolling tapered soft actuator. *Chemical Communications*, 55, 1726-1729, (2019).
2. Marina Pilz da Cunha, **Akhil R Peeketi**, Kanishk Mehta, Dirk J Broer, Ratna K Annabattula, Albert P.H.J.Schenning, Michael Debije A self-sustained soft actuator able to rock and roll. *Angewandte Chemie* (submitted)